TU Delft

Delft University of Technology

Document Version
Final published version

Licence
CC BY

Citation (APA)
Jeong, H., Lanh, K., Perez, P. G., & Vardar, Y. (2026). Multimodal Haptic Display Integrating Texture, Softness, and Thermal Rendering for Active Touch. *Advanced Materials Technologies*, Article e71463. https://doi.org/10.1002/admt.71463

Important note
To cite this publication, please use the final published version (if applicable).
Please check the document version above.

Copyright
In case the licence states “Dutch Copyright Act (Article 25fa)”, this publication was made available Green Open Access via the TU Delft Institutional Repository pursuant to Dutch Copyright Act (Article 25fa, the Taverne amendment). This provision does not affect copyright ownership.
Unless copyright is transferred by contract or statute, it remains with the copyright holder.

Sharing and reuse
Other than for strictly personal use, it is not permitted to download, forward or distribute the text or part of it, without the consent of the author(s) and/or copyright holder(s), unless the work is under an open content license such as Creative Commons.

Takedown policy
Please contact us and provide details if you believe this document breaches copyrights.
We will remove access to the work immediately and investigate your claim.

This work is downloaded from Delft University of Technology.

Check for updates

Advanced Materials Technologies

ADVANCED MATERIALS TECHNOLOGIES
www.advmattechnol.com

RESEARCH ARTICLE OPEN ACCESS

Multimodal Haptic Display Integrating Texture, Softness, and Thermal Rendering for Active Touch

Haewon Jeong | Khoa Lanh | Paulina Gallego Perez | Yasemin Vardar

Department of Cognitive Robotics, Delft University of Technology, South Holland, Netherlands

Correspondence: Yasemin Vardar (y.vardar@tudelft.nl)

Received: 27 November 2025 | **Revised:** 14 October 2026 | **Accepted:** 21 October 2026

Keywords: active touch | haptics | multimodal tactile rendering | soft haptic display

ABSTRACT

Touch allows humans to perceive fundamental cues, such as roughness, friction, softness, and temperature, that define how surfaces feel. Yet these sensations remain largely absent from digital interactions. Here, we present SensaSurf, a unified haptic display that delivers the four primary tactile modalities during active fingertip exploration. SensaSurf combines electrovibration for roughness and friction, a pneumatically actuated origami joint for stiffness, and a temperature-controlled origami bellows for thermal and contact area modulation, enabling independent control of lateral force, effective stiffness, contact area, and temperature across perceptually relevant ranges. A user study showed that these capabilities produce distinct multimodal sensations spanning major dimensions of touch. To our knowledge, SensaSurf is the first surface-based haptic display to integrate all primary tactile modalities during active bare-finger interaction, opening opportunities to study multisensory perception and to advance multimodal tactile surface rendering in digital environments.

1 | Introduction

Touch provides a direct link to the physical world, enabling humans to explore and interpret their surroundings through their fingertips. The skin senses subtle variations in surface roughness, friction, temperature, and softness—cues that support object recognition [1, 2], skilled manipulation [3], and emotional communication [4]. In digital environments, however, this rich sensory dimension is largely absent. While visual and auditory rendering now approaches perceptual realism, haptic technologies struggle to deliver high-fidelity tactile cues during natural interaction with bare fingertips [5].

Existing methods have achieved notable but isolated successes. Electrostatic [6] and ultrasonic actuation [7] enable roughness and friction rendering; Peltier elements [8, 9] evoke thermal sensations; and shape-changing devices that modulate contact-area or stiffness [10, 11] can convey softness. However, these advances are mostly confined to single tactile modalities, leaving the broader challenge of naturalistic multimodal touch—rendering multiple tactile properties through a unified, high-fidelity interface—largely unresolved. Delivering all of these cues is essential for realistic virtual interactions [12]; roughness, friction, softness, and temperature cues were found to be related to the four principal perceptual dimensions of tactile surfaces: roughness–smoothness, stickiness–slipperiness, softness–hardness, and warmth–coldness [13], each of which plays a distinct role in material recognition and perception [2, 14, 15].

Earlier efforts toward multimodal rendering explored rigid or structurally reconfigurable actuation mechanisms. Origami-based mechanisms, in particular, have been widely used to deliver

Haewon Jeong and Khoa Lanh contributed equally to this study.

This is an open access article under the terms of the Creative Commons Attribution License, which permits use, distribution and reproduction in any medium, provided the original work is properly cited.
© 2026 The Author(s). *Advanced Materials Technologies* published by Wiley-VCH GmbH

force and stiffness cues during user-initiated interaction [16, 17]. Motorized pin-array displays have been proposed to display spatial cues with variable stiffness [18], vibration [19, 20], or shear [21]. Others have combined electrovibration with vibrotactile [22] or thermal [23] feedback to deliver friction alongside vibration or temperature cues. Tool-mediated displays, such as FeelPen [24], have been also proposed to render multimodal textures through a stylus by combining electrovibration with thermal and stiffness rendering.

Recent developments in soft material technologies have introduced diverse actuation strategies that provide richer tactile cues while also conforming better to the skin. Most of these systems modulate pressure and vibration, primarily to convey softness and fine texture. Pneumatic actuation is widely employed [25–29]: inflatable silicone membranes can transmit normal force to the fingertip to render softness, while dynamic valve control can produce high-frequency vibrations that emulate fine surface roughness. By arranging these actuators in arrays, additional tactile cues, such as impact and friction forces, can also be delivered [29]. Alternatively, magnets and coils embedded in soft elastomers can generate both force and vibration via magnet displacement under time-varying magnetic fields [30], and actuators made from shape-memory alloys can stimulate skin in the normal and shear directions, creating both pressure and friction cues [31]. Other soft haptic displays use actuator arrays based on diverse principles to create spatial surface deformations, such as shape changes or macro-scale roughness, alongside vibration and pressure feedback [32–37]. More advanced systems incorporate temperature feedback, enabling multiple tactile modalities to be rendered simultaneously [38–45].

Despite these advances, most existing multimodal haptic displays can render only a subset of relevant tactile cues simultaneously (see Table 1 for a detailed comparison). Accurate softness rendering remains particularly challenging, requiring coordinated modulation of contact area and stiffness. Integrating temperature with softness, roughness, and friction adds further complexity, demanding a balance between efficient heat transfer and the mechanical constraints of multi-actuation. Moreover, such systems are body-worn or tool-mediated, limiting them to passive or indirect touch and constraining the achievable actuation range for each modality, as well as the realism of the interaction. Available surface and shape displays, in contrast, support active exploration but render at most two to three tactile modalities and do not address softness through coordinated stiffness and contact-area control.

Here, we present SensaSurf, a haptic display capable of rendering four primary and perceptually salient surface properties—roughness, friction, softness, and temperature—during active exploration with bare fingertips (Figure 1A). The device integrates three tightly coordinated mechanisms: a flexible electrovibration layer to modulate lateral forces for texture and friction rendering; a pneumatically actuated one-degree-of-freedom origami joint for stiffness control; and a temperature-controlled origami bellows that simultaneously delivers heating/cooling and modulates contact area (Figure 1B,C). Its form factor (Figure S1) accommodates a wide range of natural exploratory touch actions, including pressing, tapping, sliding, and static contact. Mechanical characterization confirms independent control over lateral force, effective stiffness, contact area, and temperature, each spanning ranges relevant to real materials and human tactile perception. Psychophysical evaluations further show that this control enables high-fidelity rendering along key perceptual surface dimensions: rough–smooth, sticky–slippery, warm–cold, and soft–hard [13].

To our knowledge, SensaSurf is the first surface-based haptic display to unify all primary tactile modalities (roughness, friction, softness, and temperature) while supporting natural, active touch. This capability provides a powerful tool for investigating how individual tactile cues combine and interact to surface perception, advancing the frontier of surface digitization. Moreover, SensaSurf opens new opportunities for immersive virtual environments, remote physical interaction, accessible computing, and expressive digital media.

2 | Results and Discussion

2.1 | Device Design and Working Principle

Our haptic display integrates three specialized modules—texture, softness, and thermal—each employing distinct actuation principles (Figure 1). Unlike previous devices, this modular architecture enables independent and simultaneous modulation of vibration, friction, pressure, contact area, and temperature, thereby reproducing tactile sensations that span the principal psychophysical dimensions of touch [13]. Below, we describe the overall design and operating principles of each module; detailed fabrication (Figure 2) and assembly (Figure 3) procedures and control protocols are provided in the Materials and Methods. Table 2 summarizes the device specifications, including dimensions, power consumption, and response characteristics for each module.

The *texture module* is located on the device's top surface (Figure 4A). It features a thin, flexible electrovibration display consisting of an insulating layer coated on a conductive base. When an alternating electric potential is applied between the conductive layer and a nearby fingertip—such as during a touch interaction—an electrostatic force is generated. This force modulates friction at the fingertip, creating dynamic texture sensations as it moves across the surface [6]. By adjusting the amplitude, frequency, and spectrum of the input electric signal, a range of texture profiles with varying sensations can be generated. As the electrostatic forces generated by electrovibration are too weak when the finger is stationary [46], texture sensations can only be reliably perceived when there is relative motion between the fingertip and the surface. Nevertheless, electrovibration is primarily suited to rendering fine textures, which naturally require finger movement for perception. Thus, although the texture module is limited to fine textures, it supports natural exploratory movements to perceive them.

Beneath the texture module, within the accordion-like origami bellows, lies the *softness module* (see Figure 4B,C). As previous studies have shown that human perception of softness depends on stiffness and contact area [10, 47, 48], we designed the softness module to address these two physical aspects by combining pneumatic and hydraulic systems to independently modulate them. The pneumatic system has a one-degree-of-freedom (1-DoF) origami joint with a pouch motor at its base. The internal

2365709x, 0, Downloaded from https://advanced.onlinelibrary.wiley.com/doi/10.1002/admt.71463 by Technical University Delft, Wiley Online Library on [23/11/2026]. See the Terms and Conditions (https://onlinelibrary.wiley.com/terms-and-conditions) on Wiley Online Library for rules of use; OA articles are governed by the applicable Creative Commons License

TABLE 1 | Comparison between SensaSurf and existing multimodal haptic devices.

	Rendered surface property								
	Roughness		Friction	Softness		Temperature			
Refs.	Vibration	Spatial deformation	Shear force	Normal force/Pressure	Contact area	Warm	Cold	Interaction	Type
[25]	+	—	—	+	—	—	—	Passive	Wearable
[26]	+	—	—	+	—	—	—	Passive	Wearable
[27]	+	—	—	+	—	—	—	Passive	Wearable
[28]	+	+	—	+	—	—	—	Passive	Wearable
[29]	+	—	+	+	—	—	—	Passive	Wearable
[30]	+	—	+	+	—	—	—	Passive	Wearable
[31]	+	—	+	+	—	—	—	Passive	Wearable
[32]	+	+	—	+	—	—	—	Passive	Wearable
[33]	—	+	+	+	—	—	—	Passive	Wearable
[34]	+	+	—	+	—	—	—	Passive	Wearable
[38]	+	—	—	—	—	+	+	Passive	Wearable
[39]	+	—	—	+	—	+	+	Passive	Wearable
[40]	+	—	—	—	—	+	—	Passive	Wearable
[41]	+	+	—	+	—	+	+	Passive	Wearable
[42]	—	—	—	+	—	+	+	Passive	Wearable
[43]	+	+	—	+	—	+	+	Passive	Wearable
[44]	+	—	—	—	—	+	+	Passive	Wearable
[37]	+	+	+	—	—	—	—	Active	Wearable
[16]	—	—	+	+	—	—	—	Active	Graspable
[17]	—	+	—	+	—	—	—	Active	Graspable
[24]	+	—	+	+	—	+	+	Active	Graspable
[35]	+	+	—	+	—	—	—	Passive	Surface
[45]	+	—	—	—	—	+	+	Passive	Surface
[18]	—	+	—	+	—	—	—	Active	Surface
[21]	+	+	+	+	—	—	—	Active	Surface
[22]	+	—	+	—	—	—	—	Active	Surface
[23]	—	—	+	—	—	+	+	Active	Surface
[36]	+	+	—	—	—	—	—	Active	Surface
**	+	—	+	+	+	+	+	Active	Surface

**SensaSurf

air pressure of the pouch motor is controlled to adjust the stiffness of the joint; inflating or deflating the pouch motor moves the origami joint up or down (Figure 4B). The joint includes a small magnet on its top surface and a magnetometer at the bottom, enabling precise monitoring and modulation of the joint's deformation and the indentation depth of the finger. A force-sensing resistor (FSR) on the joint's top surface measures contact force, enabling dynamic pressure modulation of the pouch motor in response to the interaction. The hydraulic system complements this by directing a water stream into the origami bellows. By controlling the inflow and outflow of the water, the internal volume can be adjusted in real time. Injecting water into the origami bellows causes the top membrane to bend outward, thereby increasing the area of the fingertip in contact with the surface. While direct fingertip loading cannot produce contact beyond the fingertip's own cross-sectional limit, fluid-driven deformation allows the membrane to wrap around the fingertip. As a result, increasing internal water volume increases the effective contact area, similar to touching a soft, compliant material (Figure 4C).

The *thermal module* is made of a hydraulic system (Figure 4C), which includes three water tanks: a hot tank, a cold tank, and a mixer tank. The mixer tank is divided into two chambers, namely the control chamber and the residual chamber. The water temperature is controlled by modulating the ratio of hot (45°C) to cold (0°C) water entering the control chamber. Once the target temperature is reached, the water flows through the origami

2365709x, 0, Downloaded from https://advanced.onlinelibrary.wiley.com/doi/10.1002/admt.71463 by Technical University Delft, Wiley Online Library on [23/11/2026]. See the Terms and Conditions (https://onlinelibrary.wiley.com/terms-and-conditions) on Wiley Online Library for rules of use; OA articles are governed by the applicable Creative Commons License

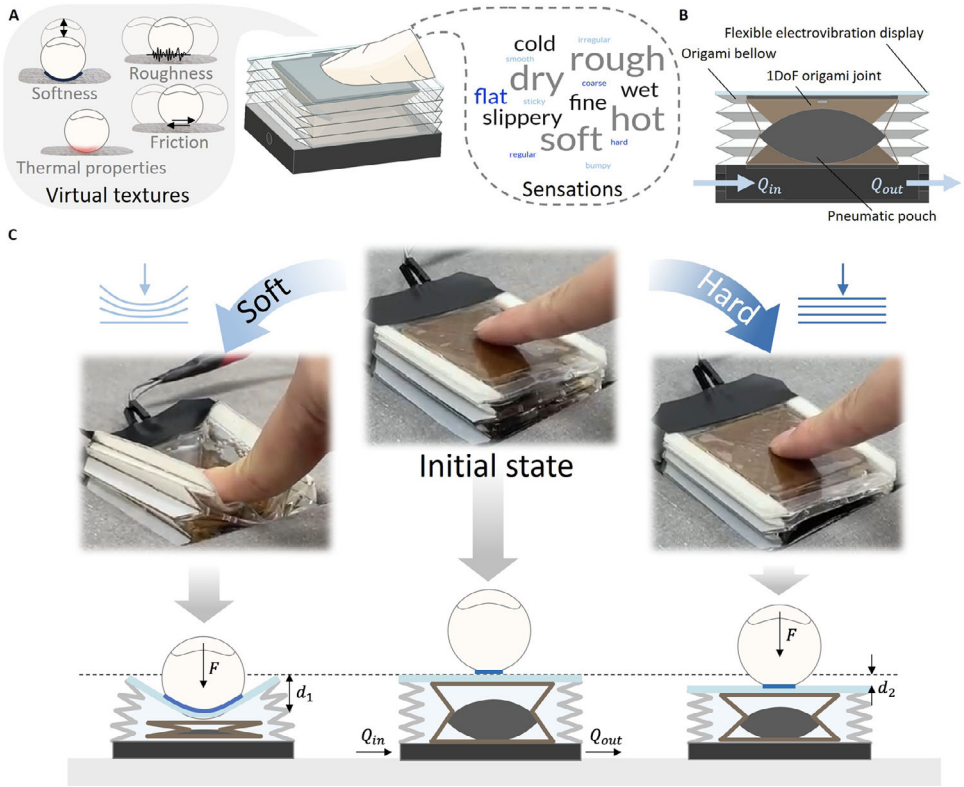


FIGURE 1 | Conceptual overview of SensaSurf. (A) Schematic of the proposed device, capable of rendering multimodal virtual textures and evoking diverse psychophysical sensations. (B) Cross-sectional view of the display. (C) Softness module operation: stiffness and contact area change in response to applied force, F. Stiffness is modulated via indentation depth by controlling pneumatic pouch pressure, while contact area is adjusted by regulating the origami bellows volume through the inflow rate Q_{in} and outflow rate Q_{out}. The resulting indentation depths (d_1 and d_2) and contact areas differ for rendered soft and hard surfaces, respectively.

bellows and then cycles back to the residual chamber before being directed to the hot and cold water tanks. Heat is transferred to the fingertip via the thin-texture module.

2.2 | Electromechanical Characterization

The operating range, control accuracy, and dynamic response of each tactile subsystem were quantified (Figure 5). The characterization included electrovibration force generation for texture rendering, force–displacement behavior and closed-loop force tracking for stiffness modulation, contact-area modulation via hydraulic volume control, and temperature tracking under static and transient target profiles. As these subsystems are integrated into the same physical stack, we also assessed potential mechanical, thermal, and electrical coupling to determine whether the four tactile dimensions could be rendered independently across their operating ranges.

The rendering capability of the texture module was evaluated by measuring the average electrostatic force in both normal and lateral directions across a range of AC voltage amplitudes and frequencies, while a participant slid their fingertip by applying constant force (0.2 N) and speed (40 mm/s) (Figure 5A; see Materials and Methods for details). Under these exploration conditions, a 200 V_{pp} input produced electrovibration forces ranging from 5 to 25 mN in the lateral direction and from 3 to 15 mN in the normal direction across the tested frequency range of 10–600 Hz. This normal force range is above the average perceptual threshold of 3 mN reported in Refs. [46, 49] (Figure 5B), ensuring that the resulting virtual roughness cues are detectable. Although these forces are lower than those reported for existing electrovibration displays based on commercial capacitive touchscreens operated at similar voltages [46], they remain sufficient to reproduce the frictional fluctuations that underlie the perception of fine textures (e.g., silk), but not coarse textures with pronounced asperities (e.g., sandpaper) [50].

Overall, both lateral and normal force magnitudes decreased systematically with lower applied voltages (Figure 5B,C). Forces exceeding the perceptual threshold were achieved at input amplitudes as low as 150 V_{pp}, indicating that effective and perceivable texture modulation can be obtained without operating at the maximum drive amplitude. At 150 and 200 V_{pp}, distinct peaks in force magnitude were observed at 28 Hz for normal force and 599 Hz for lateral force, whereas lower input amplitudes exhibited minimal frequency-dependent variation. At these higher input amplitudes, the normal-force response exhibited a band-pass behavior, with force amplitude increasing up to 28 Hz and subsequently decreasing as excitation frequency increased. However, the lateral-force response exhibited a slightly high-pass-like behavior, with force magnitude increasing with frequency before dropping sharply at 1000 Hz.

These frequency response characteristics arise from the coupled electromechanical behavior of the fingertip-display interface

2365709x, 0, Downloaded from https://advanced.onlinelibrary.wiley.com/doi/10.1002/admt.71463 by Technical University Delft, Wiley Online Library on [23/11/2026]. See the Terms and Conditions (https://onlinelibrary.wiley.com/terms-and-conditions) on Wiley Online Library for rules of use; OA articles are governed by the applicable Creative Commons License

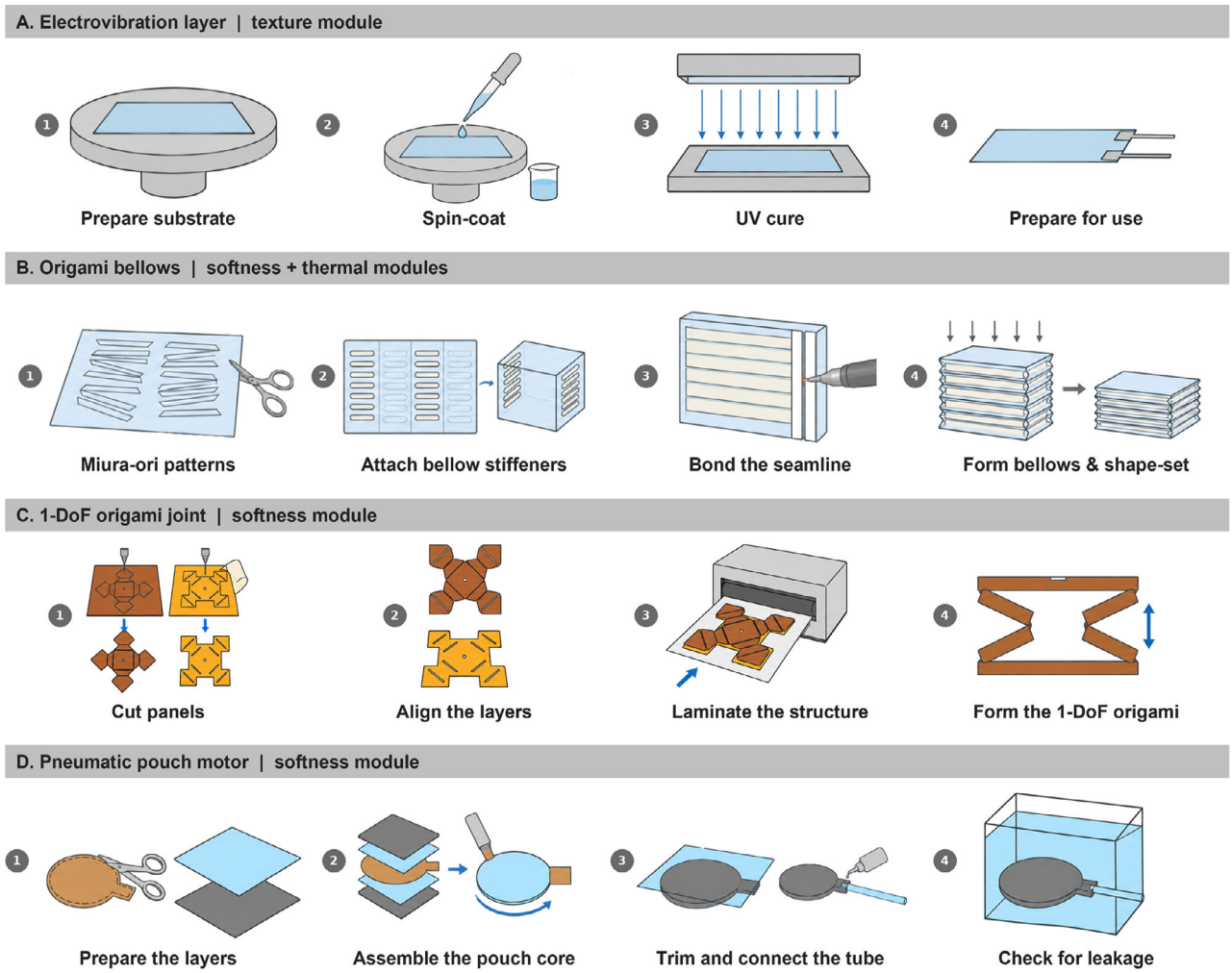


FIGURE 2 | Fabrication workflow of the SensaSurf. (A) Electrovibration layer for texture rendering, fabricated by spin-coating and UV-curing a dielectric layer on ITO-coated PET, followed by electrical connection. (B) TPU origami bellows, incorporating FR4 stiffeners for softness and thermal rendering. (C) Laminated FR4–polyimide, 1-DoF origami joint for softness modulation. (D) Heat-sealed pneumatic pouch motor fabricated from nylon, TPU, and a patterned Teflon insert. The numbered steps in each panel are described in the Materials and Methods.

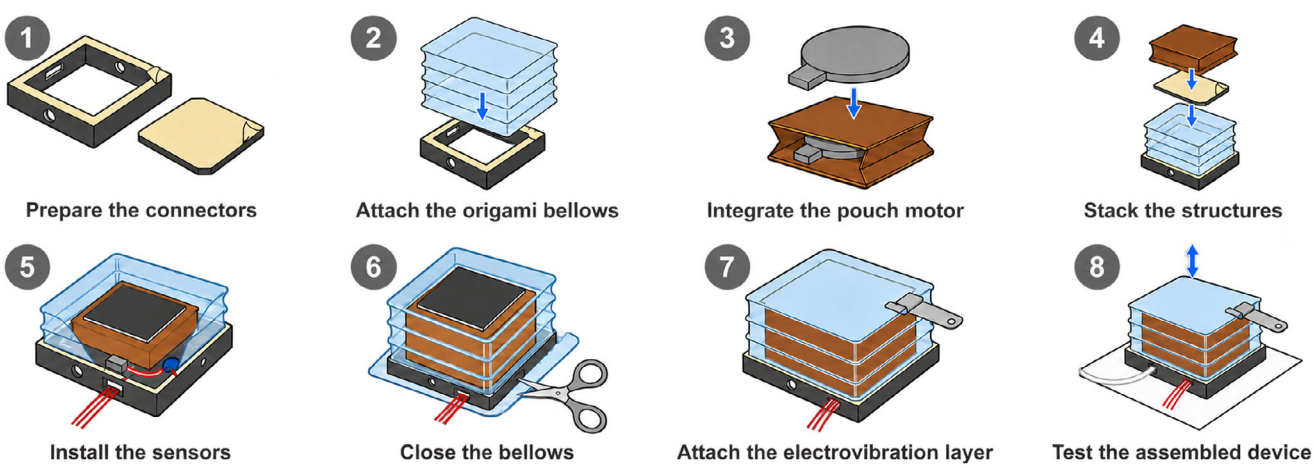


FIGURE 3 | Assembly workflow of the SensaSurf. The assembly comprises eight main steps: preparation of the 3D-printed connectors (step 1), attachment of the origami bellows (step 2), integration of the pneumatic pouch motor into the 1-DoF origami joint (step 3), stacking and bonding of the structures (step 4), installation of the thermistor, magnetometer, and force-sensitive resistor (step 5), closure and sealing of the bellows (step 6), attachment of the electrovibration layer (step 7), and testing of the assembled device for leakage, pouch inflation, sensor connectivity, and mechanical movement (step 8). Each step is detailed in the Materials and Methods.

2365709x, 0, Downloaded from https://advanced.onlinelibrary.wiley.com/doi/10.1002/admt.71463 by Technical University Delft, Wiley Online Library on [23/11/2026]. See the Terms and Conditions (https://onlinelibrary.wiley.com/terms-and-conditions) on Wiley Online Library for rules of use; OA articles are governed by the applicable Creative Commons License

TABLE 2 | Device specifications.

Module	Specification	Value
Overall Device	Dimensions	Entire system (excluding compressor and water tanks): 450×300×200 mm Electronics: 230×180×160 mm Interactive part: 50×50 mm
Texture Module	Input Voltage	up to 200 V_{pp}
	Operating Frequency	10–1000 Hz
	Lateral Force	up to 25 mN
	Normal Force	up to 15 mN
	Power	≤85 mW electrovibration layer (200 V_{pp}, 1000 Hz)[a] ≤ 120 W signal amplifier + ≤ 15 W DAQ[b]
Softness Module	Stiffness	0.5–2.0 N/mm
	Contact Area	0–250 mm^2
	Maximum Water Volume	50 ml
	Stiffness Transition Time	≈3–4 s (stiffening, 0.5 → 2 N/mm) ≈1–1.5 s (softening, 2 → 0.5 N/mm)
	Power	125 W compressor + 2× ≤ 3 W proportional valves[b] + ≈ 1 W electronics
Thermal Module	Temperature Range	15–40°C
	Maximum Rate of Change	1.32°C/s
	Hot Tank Temperature	45°C
	Cold Tank Temperature	0°C
	Response Time	40 s (steady state)
	Power	300 W heater + 120 W ice maker + 4× 19 W pumps[b] + 3× 6 W solenoid valves + ≈ 1 W electronics

[a]Upper bound on apparent power, calculated as $P = V_{\text{rms}} \times I$, with $V_{\text{rms}} = 70.7$ V and $I \leq 1.2$ mA.
[b]Rated component powers; actual power consumption is lower and varies with operating conditions and duty cycling.

[51, 52]. Electrically, this interface acts as a high-pass filter: at low frequencies, resistive leakage through the stratum corneum limits the voltage sustained across the capacitive gap, whereas at higher frequencies displacement current becomes dominant, strengthening the electrostatic coupling responsible for lateral friction [53]. Mechanically, the fingertip behaves as a low-pass filter, attenuating the transmission of higher-frequency vibrations. The observed frequency responses therefore reflect an interplay between increasing electrical coupling and decreasing mechanical transmissibility, with frequency-dependent force-sensor dynamics potentially contributing to the response at higher frequencies [51]. When reproducing finger–surface friction recorded from real textures, these frequency-dependent characteristics should be considered to ensure accurate and reliable texture rendering.

Stiffness rendering of the softness module was evaluated using a cylindrical indenter that vertically compressed the origami joint–pneumatic pouch assembly to its limit before returning to its initial position (Figure 5D; Materials and Methods for details). During testing, the displacement of the top surface was recorded as a function of the indenter force, corresponding to the target stiffness settings. The module could accurately render stiffness values from 0.5 N/mm—the lowest stiffness determined by the origami joint's hinge—to 2 N/mm, the maximum safe stiffness for interaction with the display (Figure 5E) without damaging the device. Although hysteresis was observed at 0.5 N/mm and 1.5 N/mm, the slope of the force–displacement curve remained consistent with the target stiffness. This hysteresis is attributed to mechanical clearance in the origami hinge, which permits small relative motions between folded surfaces without generating force, thereby producing a horizontal offset in the force–displacement curve without substantially altering its slope. Since compliance is perceived from the force-displacement relation [54], and compliance judgments place greater weight on the loading phase, during which the force–displacement gradient corresponds to the commanded stiffness, than on unloading [55], this clearance-type offset may have a limited effect on perceived stiffness compared with hysteresis that directly alters the force–displacement slope. Nevertheless, the extent to which this hysteresis affects perceived stiffness remains to be established.

Given that humans can discriminate stiffness differences as small as 15% when exploring with their fingertips [56], the device

2365709x, 0, Downloaded from https://advanced.onlinelibrary.wiley.com/doi/10.1002/admt.71463 by Technical University Delft, Wiley Online Library on [23/11/2026]. See the Terms and Conditions (https://onlinelibrary.wiley.com/terms-and-conditions) on Wiley Online Library for rules of use; OA articles are governed by the applicable Creative Commons License

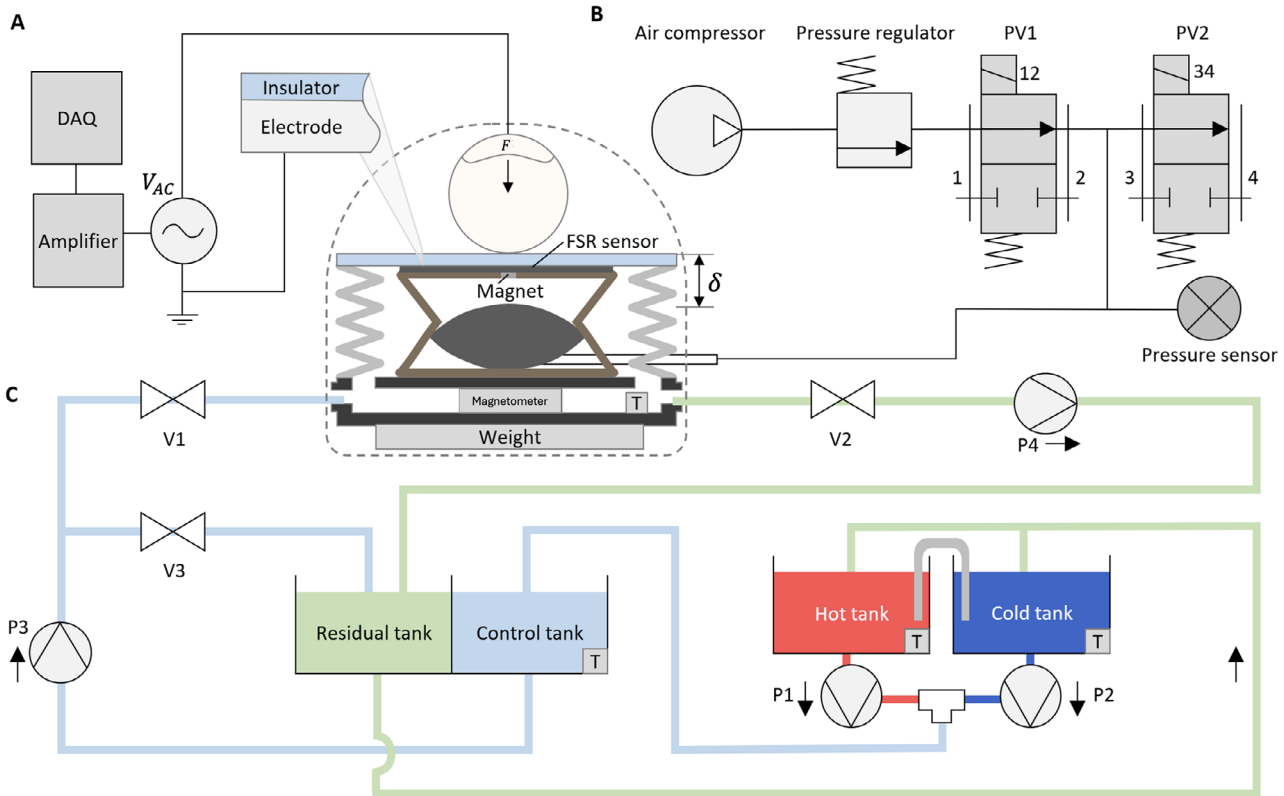


FIGURE 4 | Integrated system design of the individual tactile modules. (A) Texture module positioned on the top surface of the display, with a detailed cross-section of the electrovibration layer. (B) Pneumatic system connected to the display's pneumatic pouch. (C) Hydraulic system connected to the display's origami bellows. The hot and cold tanks are connected via a siphon tube, while a mixer tank is divided into residual and control chambers. Detailed explanations of the control for each module are provided in Materials and Methods.

covers a broad range of perceivable stiffness levels. However, its range may remain insufficient for rendering extremely soft or hard surfaces. Based on the stiffness values reported by [57], this range corresponds approximately to objects ranging from a foam ball to a rigid eraser. Furthermore, the controller accurately tracked dynamically varying target forces derived from real-time displacement measurements (Figure 5F), demonstrating reliable performance for adaptive stiffness control. The pneumatic pouch reached 90% of the commanded force change within approximately 3–4 s during stiffening and 1–1.5 s during softening.

The contact area rendering ability of the softness module was evaluated by varying the water volume inside the origami bellows and measuring the resulting contact area under fingertip forces of up to 5 N (Figure 5G; see Materials and Methods for details). Increasing water volume led to a corresponding increase in contact area for the same applied force, demonstrating precise control of contact area through volume modulation (Figure 5H). The module could render the maximum contact area (the whole fingertip) for applied forces of more than 2 N. Control accuracy was further tested using a triangular cyclic setpoint between 0 and 50 mL—selected to mimic the gradual changes in contact area typical of natural interactions. The module closely tracked the setpoint across cycles, confirming stable and responsive performance (Figure 5I).

The temperature module is designed to deliver temperature stimuli ranging from 15°C to 40°C, which lies within the comfortable range for human interaction, ensuring a pleasant user experience (Figure 5J; check Materials and Methods for details). Its rendering capability was first evaluated using step temperature profiles at a range of target set points (Figure 5K). The display showed rapid tracking for lower targets (15°C and 20°C), though steady-state errors prevented convergence within the 40 s measurement window. Intermediate set points (20°C–30°C) were tracked with the highest fidelity, whereas higher targets (35°C and 40°C) exhibited substantially longer rise times before reaching steady state. The rate of temperature change progressively decreased as the measured temperature approached the set point. The maximum observed rate at the start of heating/cooling was approximately 1.32°C/s.

As all step responses started from 25°C in Figure 5K, heating and cooling dynamics could be compared directly. The delay to reach 10% of the total temperature change was 3.5–4.7 s for heating and 5.2–5.7 s for cooling. These delays were primarily attributed to water transport from the mixing tank to the bellows. In both directions, 90% of the total temperature change was achieved within 18–24 s after the setpoint change. This broadly similar response is consistent with the use of the same PID-controlled hot- and cold-water mixing mechanism for both heating and cooling, so that switching between them involves reversing the setpoint rather than changing the actuation mode.

To evaluate the thermal module under conditions resembling real material interactions, we used the transient temperature response

2365709x, 0, Downloaded from https://advanced.onlinelibrary.wiley.com/doi/10.1002/admt.71463 by Technical University Delft, Wiley Online Library on [23/11/2026]. See the Terms and Conditions (https://onlinelibrary.wiley.com/terms-and-conditions) on Wiley Online Library for rules of use; OA articles are governed by the applicable Creative Commons License

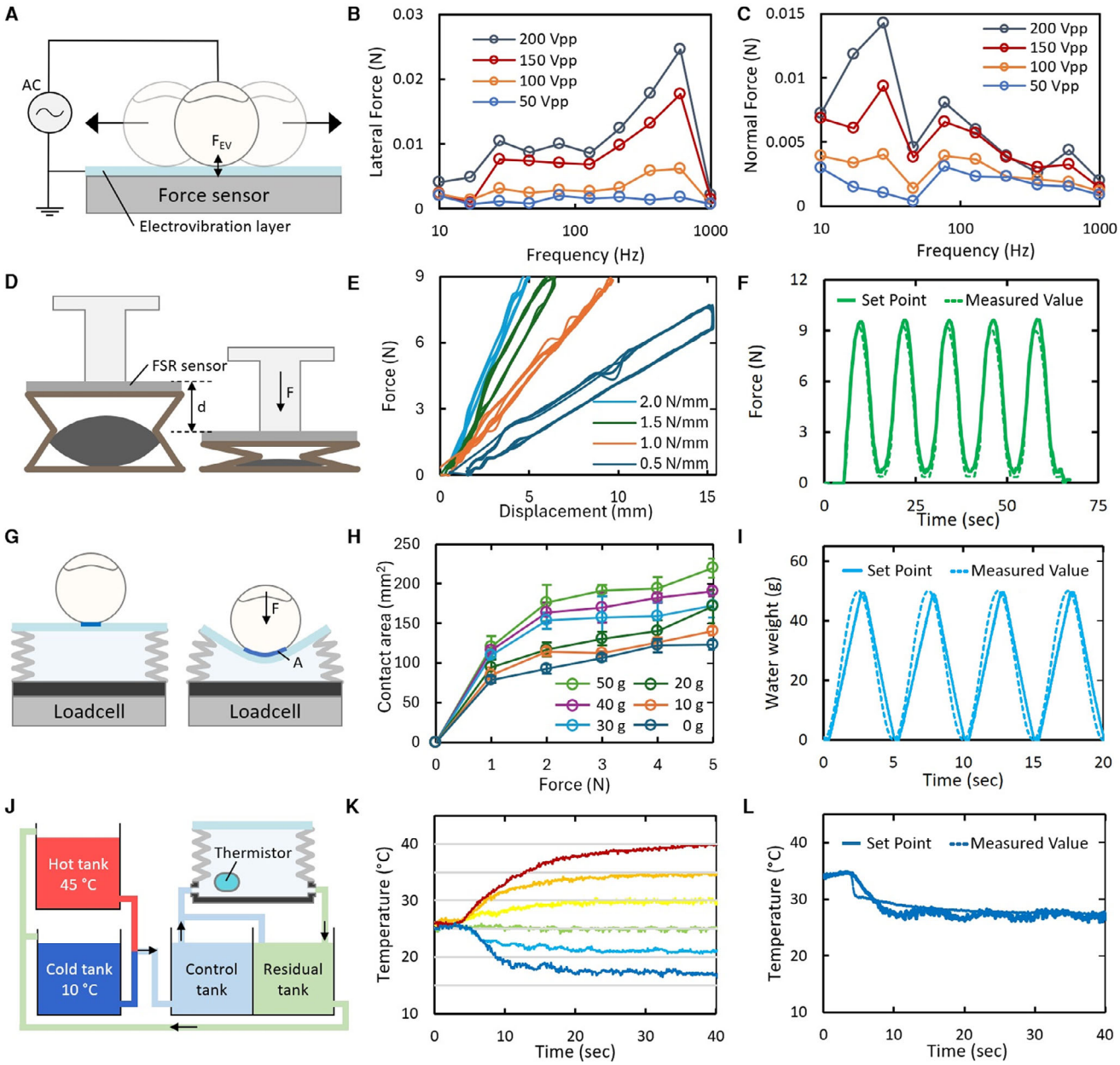


FIGURE 5 | Results of tactile module characterization. (A) Experimental setup for characterizing the texture module. (B,C) Amplitudes of lateral and normal electrovibration forces measured by the force sensor as a function of input voltage and frequency. Each curve corresponds to a different input voltage amplitude. (D) Experimental setup for characterizing stiffness modulation. (E) Measured stiffness of origami joint with pneumatic pouch actuator for different target stiffness values. (F) Comparison of the setpoint force and measured forces of the origami joint with pneumatic pouch actuator. (G) Experimental setup for evaluating contact area modulation. (H) Measured contact area of the origami bellows for different target water weights. (I) Comparison of the setpoint and measured water weights of the origami bellows. (J) Overview of the temperature module. (K) Temperature responses for different target temperatures, indicated by gray horizontal lines. Red and blue curves indicate heating and cooling, respectively. (L) Comparison of the setpoint and measured temperatures of the origami bellows.

of a metal plate extracted from Ref. [50] as a reference (Figure 5L). The display was unable to reproduce the steep initial temperature change characteristic of metal and exhibited a noticeable delay, indicating that the resulting thermal sensation would differ from that of direct contact with a real sample. These results suggest that the module is better suited for rendering stable, steady-state temperatures than rapidly varying thermal profiles with sharp fluctuations.

The same trace also illustrates a transition from heating to cooling, as the display was preheated to approximately 34°C before the reference profile was applied. The display began responding after approximately 5 s and completed the 10%–90% portion of the 6°C temperature drop in approximately 4 s. Based on these measurements and the step responses in Figure 5K, a reversal spanning the full 15°C–40°C operating range is estimated to require approximately 25–30 s.

2365709x, 0, Downloaded from https://advanced.onlinelibrary.wiley.com/doi/10.1002/admt.71463 by Technical University Delft, Wiley Online Library on [23/11/2026]. See the Terms and Conditions (https://onlinelibrary.wiley.com/terms-and-conditions) on Wiley Online Library for rules of use; OA articles are governed by the applicable Creative Commons License

As the tactile modules share mechanical, thermal, and electrical pathways, cross-modal coupling was evaluated across the operating ranges (see Materials and Methods, and Figures S2 and S3 for details). These evaluations showed that hydraulic volume affected pneumatic actuation, but this effect was compensated for by the closed-loop stiffness controller, preserving the full stiffness range of 0.5–2.0 N/mm. Temperature changes produced negligible softening of the TPU structure. Curvature induced by the hydraulic and pneumatic modules changed the electrovibration force by at most ≈7%, while electrovibration contributed less than 1.5% to the forces used for stiffness rendering. Contact-area control was negligibly affected by pouch pressure or thermal expansion of the water. Pneumatic operation changed the rendered temperature by less than 0.01,° C. Electrovibration caused no measurable water heating or meaningful bias in the thermistor or magnetometer readings. Temperature-induced changes in displacement sensing remained below the stiffness discrimination threshold [56]. Together, these results demonstrate that the four tactile dimensions can be controlled with limited cross-modal interference within the selected operating ranges.

2.3 | Perceptual Validation

A psychophysical study with 13 participants was conducted to evaluate the rendered sensations by SensaSurf. Participants rated 64 virtual surfaces, each defined by a unique combination of six parameters—amplitude, frequency, irregularity, stiffness, contact area, and temperature—using adjective pairs on a 9-point Likert scale (e.g., rough–smooth, warm–cold; see Figure 6A and Methods for details). During each trial, participants explored the surfaces through static touch, sliding, and pressing motions before providing ratings.

Principal component analysis (PCA) revealed four distinct perceptual dimensions of the surfaces rendered by SensaSurf (Figure 6B). Factor analysis showed that the first component accounted for 33.8% of the variance and was dominated by the adjective pairs *flat–bumpy* and *rough–smooth*, with *fine–coarse* and *regular–irregular* also contributing strongly. This axis likely corresponds to perceptual roughness. The second component explained 29.5% of the variance and was characterized by *wet–dry* and *hot–cold*, reflecting thermal and moisture-related sensations. The third component (22.9% of the variance) was defined by *sticky–slippery*, consistent with perception of surface friction. Finally, the fourth component (13.8% of the variance) was represented by *hard–soft*, capturing the perception of softness.

The correlation matrix illustrates the relationships between physical parameters and adjective pairs (Figure 6C). Temperature shows a strong correlation with *wet–dry* and *hot–cold*, as expected, since wetness is often linked to thermal sensation [58]. It also shows moderate associations with *fine–coarse*, *sticky–slippery*, and *rough–smooth*, likely reflecting the perceptual bias toward metallic or glassy surfaces, which are often judged as fine, slippery, and smooth [59].

Frequency and amplitude are moderately correlated with *fine–coarse*, *sticky–slippery*, *flat–bumpy*, and *rough–smooth*. Among the values in the two selected pairs of parameters (28 and 128 Hz, 150 V_{pp} and 200 V_{pp}), higher frequency and lower amplitude tend to produce smoother and slippier surface sensations, while lower frequency and higher amplitude correspond to coarser, rougher, and stickier surfaces. Irregularity shows a moderate association with *flat–bumpy*. This result can be explained by the spectral content of the signal: flat surfaces resemble a combination of many low-amplitude, high-frequency signals, whereas bumpy surfaces are characterized by dominant, higher-amplitude low-frequency components.

Stiffness shows a strong correlation with *hard–soft*, consistent with their shared dependence on force perception. Contact area exerts a weaker influence, showing modest associations with *hard–soft* and *flat–bumpy*. These results suggest that softer objects, being more compliant, produce a larger fingertip contact area. Likewise, in real-world bumpy surfaces, texture geometry can increase the effective contact area, which may partly explain the observed effects.

2.4 | Limitations and Future Directions

Despite the rigorous fabrication methods and experimental design, our study has several limitations that could be addressed in future work.

One limitation concerns the rendering capabilities of the SensaSurf. The texture module generates fine-scale tactile sensations through electrovibration and therefore requires relative motion between the finger and surface. Consequently, SensaSurf cannot reproduce textures dominated by macro-scale roughness. Future designs could integrate complementary technologies, such as shape-changing materials [32, 36, 42], to broaden the range of reproducible texture sensations.

The softness module provides a broad range of mechanical responses but cannot reproduce extremely soft or hard surfaces. Achieving a substantially wider softness range would require reconsideration of the overall mechanism design and material selection. In addition, although the observed hysteresis did not substantially alter the force–displacement slope during loading, its effect on perceived stiffness remains to be systematically evaluated.

Although the thermal module reliably renders steady-state surface temperatures within a comfortable range (15°C–40°C), its response speed limits its ability to reproduce of rapid thermal transients characteristic of certain real material contacts. When a fingertip contacts a thermally conductive material, such as metal or ceramic, heat flux develops within fractions of a second, providing an important cue for material discrimination [8, 14]. The fluid transport delay inherent to the hydraulic system limits the module's dynamic performance. The maximum observed temperature-change rate was approximately 1.32°C/s, which is insufficient to reproduce such rapid thermal signatures, as also demonstrated by the tracking results in Figure 5L. Furthermore, reversing the temperature across the full operating range requires approximately 25–30 s, limiting the rendering of rapidly alternating thermal cues. This limitation consequently restricts both the range of materials whose thermal signatures can be reproduced with SensaSurf and the variety of applications it can support.

2365709x, 0, Downloaded from https://advanced.onlinelibrary.wiley.com/doi/10.1002/admt.71463 by Technical University Delft, Wiley Online Library on [23/11/2026]. See the Terms and Conditions (https://onlinelibrary.wiley.com/terms-and-conditions) on Wiley Online Library for rules of use; OA articles are governed by the applicable Creative Commons License

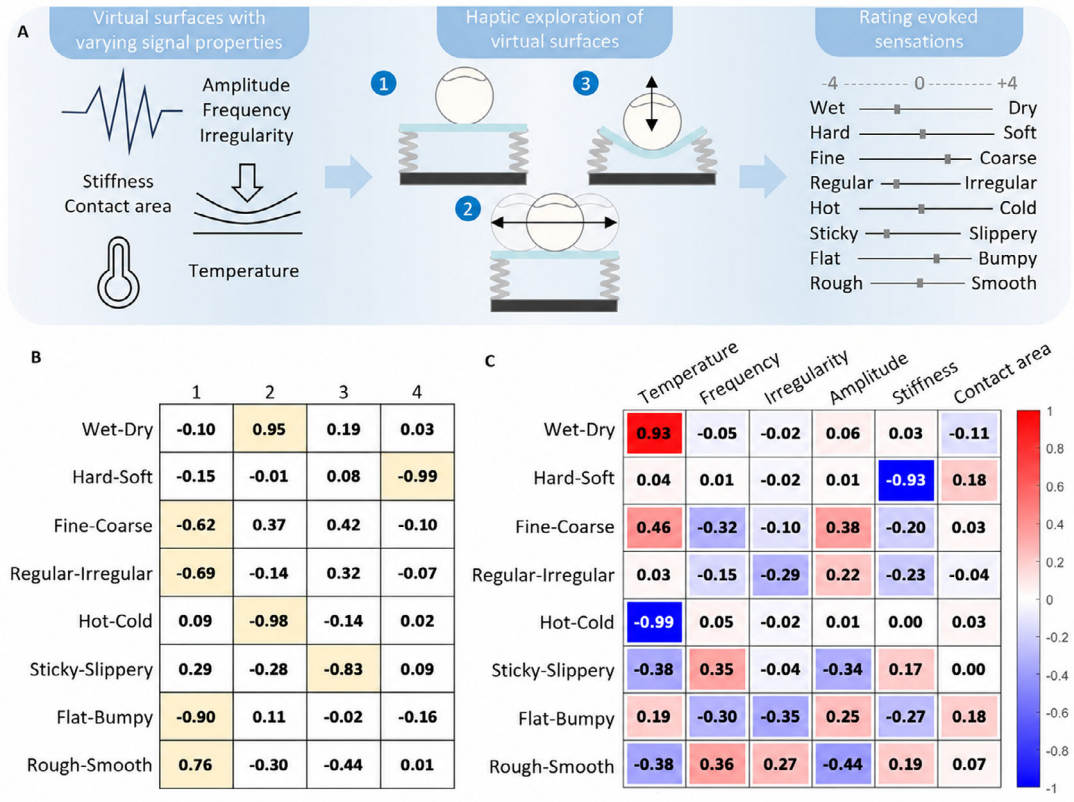


FIGURE 6 | Results of the perceptual evaluation. (A) Illustration of the experimental protocol of the psychophysical study. 64 virtual surfaces with varying signal properties are displayed. Participants explored SensaSurf through static touch, sliding, and pressing motions. Then, they rated the perceived sensations using eight adjective pairs. (B) Principal component analysis of perceptual ratings with factor loadings. (C) Correlations between adjective pairs and physical parameters.

Future designs could therefore prioritize faster thermal transients. Flexible Peltier-based thermoelectric elements offer a promising approach by enabling direct solid-state heat transfer without the transport delay associated with fluidic systems. Recent advances in thin-film form factors have improved their compatibility with compliant haptic surfaces [60]. Thermoelectric polymer films or phase-change materials integrated into the contact layer could offer alternative approaches for rapid localized heating and cooling while maintaining mechanical compliance [61–63]. Combining a fast-response thermal element with the existing hydraulic system for steady-state temperature control could ultimately enable a hybrid architecture capable of reproducing a broader range of material-specific thermal profiles.

In this study, we focused primarily on the design and fabrication of SensaSurf and evaluated its electromechanical and perceptual capabilities. However, we did not assess its ability to reproduce tactile sensations of real textures. Such an evaluation would require an overarching rendering methodology for each tactile modality, similar to the approach proposed in Ref. [41]. We also did not investigate perceptual interactions between modalities or their potential effects on the rendering of surface sensations. Developing multimodal rendering strategies and characterizing these perceptual interactions could be important directions of future work.

Moreover, the robustness of the device could be further improved. Although the origami bellows was designed with a safety factor of three relative to their maximum operating volume to prevent overfilling and remained effectively sealed throughout the experiments, small residual air bubbles occasionally remained after water filling. Residual air bubbles were not observed to substantially alter thermal rendering or tactile perception under the experimental conditions, although their potential effects on device performance were not systematically quantified. In addition, the thin insulating layer also presents a potential durability concern. To mitigate this risk, the resin could be replaced with a more wear-resistant insulating material that maintains the same (1 μm) thickness and dielectric properties, thereby preserving electrovibration performance while improving durability. Wear testing could further establish usage-duration limits and replacement intervals for the insulating layer, while real-time capacitance monitoring could provide an early indication of degradation before the layer reaches a critical thickness. Finally, hardware-level safeguards, such as series current-limiting resistors or ground-fault-style detection circuitry, could provide an additional layer of protection independent of the condition of the insulating layer.

Finally, further miniaturization of SensaSurf is needed before practical deployment. While the present system can be assembled in a relatively compact configuration for demonstration (Figure S1), it remains a laboratory-scale prototype that relies on external pumps and tanks and is therefore not directly suitable for portable, wearable, or commercial VR/AR integration. Practical deployment would require substantial miniaturization of both

2365709x, 0, Downloaded from https://advanced.onlinelibrary.wiley.com/doi/10.1002/admt.71463 by Technical University Delft, Wiley Online Library on [23/11/2026]. See the Terms and Conditions (https://onlinelibrary.wiley.com/terms-and-conditions) on Wiley Online Library for rules of use; OA articles are governed by the applicable Creative Commons License

the device itself and its supporting components, together with integration of the currently external fluidic hardware into a compact form factor.

3 | Conclusions

To our knowledge, SensaSurf is the first surface-based haptic display to integrate the rendering of all primary tactile modalities—roughness, friction, softness, and temperature—within a single platform during active finger exploration. It combines a flexible electrovibration layer for texture and friction, a pneumatically actuated one-degree-of-freedom origami joint for stiffness modulation, and a temperature-controlled origami bellows for contact area and surface-temperature modulation. By independently modulating lateral force, stiffness, contact area, and temperature, SensaSurf supports versatile rendering across key perceptual dimensions, including rough–smooth, warm–cold, sticky–slippery, and hard–soft. This integration provides a platform to investigate multisensory perception and establishes a foundation for future haptic interfaces in immersive digital technologies.

4 | Materials and Methods

4.1 | Device Fabrication

The fabrication and integration workflow of SensaSurf is summarized in Figures 2 and 3. Figure 2 illustrates the fabrication of the four main components: the electrovibration layer, origami bellows, 1-DoF origami joint, and pneumatic pouch motor. Figure 3 shows the subsequent integration of these components with the sensing elements and connectors to form the complete multimodal display. Detailed fabrication and assembly procedures are described below.

The flexible electrovibration display of the texture module (Figure 2A) consists of a 1 μm insulating layer spin-coated onto a 50 μm ITO-coated PET film (Biotain Crystal) [64]. The thickness of this PET substrate was selected to provide sufficient flexibility for conformity to the finger during contact. The substrate was first cut to the required dimensions, cleaned it with isopropyl alcohol, and secured flat on the spin-coater (Figure 2A, step 1). UV-curable epoxy resin (Wilsor) was diluted 1:1 with acetone to reduce its viscosity, deposited on the film, and spin-coated at 3000 rpm for 40 s using smooth acceleration and deceleration ramps (Figure 2A, step 2). The coated film was then cured under a UV lamp for 2–3 min, yielding an insulating layer approximately 1 μm thick (Figure 2A, step 3).

Electrical connection to the ITO electrode was established through a small slit in the film. A crimp connector was inserted into the slit and bonded with conductive ink. After drying, the electrical joint was reinforced with a second application of conductive ink and insulated using tape separated from the conductive layer by a non-adhesive interlayer. This interlayer was used as direct contact between the adhesive tape and the ITO coating can cause delamination. The integrity of the coating and electrical connection was inspected before use (Figure 2A, step 4). This display was actuated by an alternating voltage signal generated by a data acquisition card (NI 9264, National Instruments) operated at a sampling rate of 10 kHz. The signal was amplified using a high-voltage amplifier (9200 A, Tabor Electronics) and applied to the conductive layer.

The origami bellows shared by the softness and thermal modules (Figure 2B) were fabricated from a 0.1–0.2 mm thermoplastic polyurethane (TPU) sheet folded into a Miura–ori–derived bellows pattern [65]. Flexible TPU segments were reinforced with 0.1 mm FR4 panels bonded to their faces on opposing sides, such that deformation was localized at the fold lines and the bellows could bend. The two-dimensional pattern was parameterized by the segment width, segment height, and number of folds n. The fold tolerance between adjacent segments was set to ≈1.5× the equally distributed collapsed-stack spacing, $t \approx 0.75\,s/(n-1)$, where s denotes the collapsed thickness of the laminated stack. This tolerance allowed the bellows to fully compress without interference. The usable stroke was conservatively limited to half of the fully extended pattern height.

The FR4 stiffeners, backed with double-sided adhesive, were first cut according to the two-dimensional origami pattern. A TPU sheet sufficiently large to accommodate the complete bellows pattern was also cut (Figure 2B, step 1). Half of the stiffeners were aligned and bonded to two non-adjacent columns of the pattern marked on the flat TPU sheet. The sheet was then folded into an envelope with aligned edges, enclosing the stiffeners, and closed with a 2–3 mm seam margin (Figure 2B, step 2). The seam was thermally welded at 140°C using an iron or a fine-tip heating tool, while the remaining regions were masked with PTFE sheets [66]. A second welding pass was performed over a cylindrical backing to ensure a continuous fusion line (Figure 2B, step 3). After the remaining stiffeners were bonded, the laminated sheet was folded along the predefined pattern into the three-dimensional bellows shape and heat-set using an iron at 80°C for 20 min. The resulting folds, symmetry, and sealed seams were then inspected (Figure 2B, step 4).

The pneumatic system, comprising the origami joint and pouch motor, is part of the softness module and controls the display's mechanical stiffness. The 1-DoF origami joint (Figure 2C) consists of rigid FR4 panels (0.2 mm, RS) connected by flexible polyimide hinges (Kapton, 0.5 mm, Winway Electronics). Both layers were laser-cut from parameterized two-dimensional patterns. The FR4 sheet was cut to the panel pattern, while thermal adhesive tape was applied to the polyimide sheet and cut to the corresponding hinge pattern. Slits in the polyimide pattern localized bending at the hinge lines. The gap between adjacent FR4 panels was maintained at ≈0.2 mm to minimize lateral play in the structure (Figure 2C, step 1).

The FR4 panels were positioned on the adhesive-backed polyimide layer such that the openings between adjacent panels formed the flexible hinges (Figure 2C, step 2). The assembly was covered with PTFE protection sheets and bonded through repeated passes in a laminator until the FR4 and polyimide layers were firmly joined through the thermal adhesive tape (Figure 2C, step 3). While still warm, the laminated sheet was folded along the hinges into the three-dimensional joint and held in position until it cooled, setting the shape. The joint motion was then

2365709x, 0, Downloaded from https://advanced.onlinelibrary.wiley.com/doi/10.1002/admt.71463 by Technical University Delft, Wiley Online Library on [23/11/2026]. See the Terms and Conditions (https://onlinelibrary.wiley.com/terms-and-conditions) on Wiley Online Library for rules of use; OA articles are governed by the applicable Creative Commons License

verified, and a 3 mm radius neodymium magnet was embedded in the top surface for displacement sensing (Figure 2C, step 4). The panel height was selected such that the usable stroke was ≈75% of the fully extended height, providing a margin against overextension.

The origami joint and the device's top surface are mechanically decoupled. The origami joint provides vertical motion through its single degree of freedom, while the top surface can undergo horizontal deformation independently during finger exploration. Thus, horizontal deformation of the top surface induced by finger sliding does not constrain the vertical motion of the origami joint.

The pneumatic pouch motor (Figure 2D) was fabricated from nylon fabric, TPU sheets, and a PTFE insert cut according to the pouch pattern, which comprised a 37 mm-diameter circular cavity with a tube inlet (Figure 2D, step 1). The nylon fabric, TPU sheet, and patterned PTFE insert were stacked in this order and heat-pressed at 180°C, working progressively from one edge toward the other to minimize air entrapment. The PTFE insert served as an anti-welding mask to define the internal cavity (Figure 2D, step 2). After heat pressing, the excess material was trimmed, and additional TPU sheets were heat-pressed onto both faces at 180°C to increase the burst strength. The composite was then cut to its final shape, leaving a 0.5–1 mm seal margin. A 2 mm diameter PTFE tube was inserted into the inlet and bonded using cyanoacrylate adhesive (Loctite 406) (Figure 2D, step 3). Finally, the pouch was inflated using an air compressor and submerged in water to inspect for air leakage before installation (Figure 2D, step 4).

The individual components were integrated into the complete SensaSurf device following the assembly sequence shown in Figure 3. The device was assembled around two 3D-printed PLA connectors: a rectangular rim (connector 1) with feed-through holes for the sensor wiring and a flat platform (connector 2) supporting the origami joint. After printing, double-sided adhesive was applied to the attachment surfaces of both connectors (Figure 3, step 1).

Connector 1 was inserted into the bottom of the origami bellows and bonded with the double-sided adhesive. The TPU margin was then wrapped around the base of the connector, and the corners heat-sealed at 140°C (Figure 3, step 2). The pouch motor was placed inside the 1-DoF origami joint and secured with double-sided adhesive (Figure 3, step 3). The joint was bonded to connector 2, which was aligned and bonded onto connector 1 (Figure 3, step 4).

The sensing elements were subsequently installed (Figure 3, step 5). The thermistor was routed through a hole in connector 1, and the opening was sealed with silicone adhesive. The magnetometer was enclosed in a sealed TPU pouch, inserted through the rectangular opening of connector 1, and similarly sealed with silicone adhesive. For the FSR, thin lead wires were soldered to pins clamped through the trimmed electrode tails. The solder joints were insulated with silicone, and the sensor was enclosed in a sealed TPU pouch before being mounted on the top plate of the origami joint. Its wires were routed through connector 1 with sufficient slack to accommodate the joint's full stroke, and the feed-through was sealed with silicone adhesive. This sheathing-and-sealing procedure isolated all sensing elements from the water circuit.

The bottom of the bellows was closed by heat-pressing a TPU sheet onto the wrapped margin, while the excess TPU at the top was folded, sealed, and trimmed (Figure 3, step 6). The electrovibration layer was positioned on top of the bellows and secured using the remaining TPU margin and double-sided adhesive. The excess TPU flaps at the top were then thermally welded and trimmed (Figure 3, step 7).

Finally, the assembled display was filled with water and inspected for leaks. Pouch inflation, sensor connections, and structural movement were also verified. Any detected leak path were sealed with silicone or cyanoacrylate adhesive before use (Figure 3, step 8).

4.2 | Device Control

The display stiffness is controlled by regulating the pressure of the pouch motor, whose changing volume modulates the height of the origami joint (Figure 4B). An air compressor supplies air to the pressure regulator, which maintains a consistent pressure up to the maximum input level. The air then flows through two proportional valves (PV1 and PV2—FESTO, VPWS), which control the inflow and outflow of air to the display, respectively. The pouch motor is connected between PV1 and PV2, with a pressure sensor (Honeywell, ABPDANN060PGAA5) continuously monitoring its internal pressure. A PID (Proportional–Integral–Derivative) controller is used to regulate the display's stiffness by measuring the force and distance of the display from the FSR sensor and the magnetometer individually; see Supporting Information for details. Given that stiffness is defined as force divided by distance, the required force to achieve a specific stiffness at a given distance can be calculated. This target force is used as a setpoint to compute the control error. When the error is positive, a pulse-width modulation (PWM) signal is generated for PV1, adjusting the pouch motor's inflow. Conversely, if the error is negative, the PWM signal for PV2 is computed to regulate the outflow. To avoid overshooting and for safety, PWM computation is restricted to instances when the distance is positive. The system operates at a sampling rate of 10 ms, controlled by a microcontroller (Teensy 4.1).

The softness and thermal modules share the hydraulic system formed by the water encapsulated within the origami bellows, which controls the modulation of contact area and display temperature. It regulates water volume and temperature through three water tanks: a hot tank, a cold tank, and a mixer tank, each equipped with thermistors (T) for precise temperature monitoring (Figure 4). The hot tank holds 2 liters of water heated to 45°C using a 300 W immersion heater, while the cold tank, incorporating an ice maker (PR407IB, Primo), maintains 2 liters of water at 0°C. A stable low temperature is achieved at the ice-to-water phase change, as ice cubes are produced and continuously melt in the water bath.

The water temperature in the mixer tank's control chamber is regulated by adjusting the inflow rates of the hot and cold

2365709x, 0, Downloaded from https://advanced.onlinelibrary.wiley.com/doi/10.1002/admt.71463 by Technical University Delft, Wiley Online Library on [23/11/2026]. See the Terms and Conditions (https://onlinelibrary.wiley.com/terms-and-conditions) on Wiley Online Library for rules of use; OA articles are governed by the applicable Creative Commons License

water using a PID controller. This volume of temperature-monitored water is then directed to the origami bellows, where it contacts the user's fingertip. Two temperatures were monitored with thermistors placed at distinct points along the water line: the Mixer temperature, measured inside the control chamber after the hot and cold flows were combined, and the display temperature, measured inside the origami bellows. The temperature data from all the thermistors were recorded at a sampling rate of 10 ms. Pumps P1 and P2 draw water from the hot and cold tanks into the mixer tank's control chamber, while pump P3, positioned at the outlet, maintains a minimal water level to optimize the heat capacity. The hot and cold tanks, each with a maximum volume of 2 liters, feed into the mixer tank, which consists of two 300 mL chambers.

The hydraulic system regulates the water volume to modulate the contact area. Pumps P3 and P4, positioned at opposite ends of the display, operate at a constant speed. The solenoid valves V1 and V2 are activated sequentially to increase or decrease the water volume. A load cell beneath the display monitors water volume by measuring its weight. The weight values were sampled at 100 ms intervals to ensure adequate signal stabilization. A PID controller was used to control the activation of valves V1 and V2 so that the display could obtain the target water volume inside. The outflow from the display is directed to the residual chamber of the mixer tank before being recirculated to the hot or cold tank by pump P4. The residual tank is elevated above the hot and cold tanks, allowing water to flow back naturally through a siphon tube and ensuring equal water levels. When controlling water volume, prolonged or repeated flow blockages can cause the water level in the control chamber to rise, potentially disrupting temperature control or causing overflow. To mitigate this, solenoid valve V3 is installed parallel to V1, allowing excess water from the control chamber to bypass the display and flow directly into the residual chamber.

During water filling, eliminating trapped air was challenging; small bubbles occasionally remained inside the origami bellows. These bubbles rarely accumulated beneath the central contact area and instead tended to migrate toward the highest regions of the structure. During deformation of the top surface to simulate soft-object indentation, the residual bubbles were displaced toward the corners rather than the sensing region. No noticeable effects of residual air pockets on thermal rendering or tactile perception were observed during the experiments.

The power requirements of SensaSurf are summarized in Table 2. The complete laboratory-scale system has a total rated power of less than 0.8 kW, although the actual power consumption during operation is lower because the compressor, heater, and ice maker are duty-cycled and the pumps and valves operate intermittently. The electrovibration interface itself requires substantially less power, with an estimated upper bound on apparent power of 85 mW at 200 V_{pp} and 1000 Hz and approximately 11 mW under the conditions of the perceptual study.

4.3 | Characterization Experiments

4.3.1 | Texture Module

A custom force-sensing setup was developed for this experiment (Figure 5A). During testing, a participant applied a force of 0.2 N to the electrovibration film placed on a plexiglass substrate of the same size. The forces were measured using a 6-axis force sensor (Nano43) installed beneath the substrate. The participant then slid their finger horizontally back and forth at a target speed of 40 mm/s. To ensure consistent motion, an infrared touch sensor tracked the finger's position and projected the trajectory onto a monitor. An animation of a cube moving at the target speed and along the desired trajectory provided visual feedback, allowing the participant to match the intended movement. Four voltage amplitudes (50, 100, 150, and 200 V_{pp}) and ten frequencies, logarithmically spaced from 10 to 1000 Hz (10, 17, 28, 46, 77, 129, 215, 359, 599, and 1000 Hz), were tested. The resulting electrovibration forces (lateral and normal) were calculated using the method described in Ref. [46].

4.3.2 | Softness Module

A cylindrical indenter with a 9 mm radius was used for these measurements. The indenter cycled vertically, fully compressing the origami joint before returning to its initial position. Displacement and normal force were recorded to quantify stiffness control (Figure 5D), with target values ranging from 0.5 to 2.0 with 0.5 N/mm increments. The controller's accuracy was assessed by tracking the target force, which was dynamically computed from real-time displacement measurements (Figure 5F).

The stiffness transition time was characterized from step responses of the tuned closed-loop controller. The commanded stiffness was stepped between settings corresponding to a 7.5 N change in pressing force at a constant indentation of 5 mm, equivalent to a stiffness transition from 0.5 to 2.0 N/mm. The FSR force used by the 10 ms control loop was logged during each step ($n = 3$ per direction). Transition time was defined as the time from the step command to 90% of the steady-state force.

The contact area was measured by applying ink to the top surface of the bellows, after which the experimenter pressed their fingertip onto the surface, then onto paper to produce a stamped fingerprint. The fingerprints were analyzed in ImageJ to quantify contact area. Water volume was varied from 0 to 50 g—the maximum safe volume—while forces from 0 to 5 N were applied, with measurements recorded at each force level (Figure 5H).

4.3.3 | Thermal Module

For step response characterization, six constant temperature profiles were applied to the display: 15°C, 20°C, 25°C, 30°C, 35°C, and 40°C, with an initial display temperature of 25°C for all cases (Figure 5K). For material-based temperature tracking, the profile of a metal plate was extracted from [50] and used as the target

2365709x, 0, Downloaded from https://advanced.onlinelibrary.wiley.com/doi/10.1002/admt.71463 by Technical University Delft, Wiley Online Library on [23/11/2026]. See the Terms and Conditions (https://onlinelibrary.wiley.com/terms-and-conditions) on Wiley Online Library for rules of use; OA articles are governed by the applicable Creative Commons License

trajectory (dashed line in Figure 5L). The display temperature was recorded and compared against the target profile during the experiments.

4.3.4 | Cross-Modal Coupling

4.3.4.1 | Coupling Between Hydraulic and Pneumatic Actuators for Stiffness and Contact Area Rendering. The coupling between the hydraulic and pneumatic actuators for stiffness rendering was characterized in an open-loop configuration. The display was disconnected from the control electronics. Then, the water volume inside the origami bellows was manually set to 0, 25, or 50 g (empty, intermediate, and maximum safe volumes). The pouch pressure was independently set to 0, 100, or 200 kPa using the pressure regulator. For each combination ($n = 4$), a cylindrical indenter (9 mm radius) compressed the display at 0.5 mm/s (acceleration of 20 mm/s^2) up to a displacement of 5–10 mm or a force limit of 10 N, whichever occurred first. Position and normal force were recorded at 10 kHz and force–indentation curves were analyzed over 0–5 mm of indentation (Section S1.1 and Figure S2). Stiffness was quantified as the secant stiffness at 1.25 mm indentation, corresponding to the largest indentation reached in all conditions. The interaction between water volume and pouch pressure was assessed using a two-way ANOVA (water × pressure); see Supporting Information for detailed analysis.

The potential influence of pouch pressure on the rendered contact area was considered from three aspects. First, the pneumatic and hydraulic circuits are physically separate: the pouch is a closed air circuit and does not exchange volume with the water. The water volume, which determines the membrane wrap, is regulated by weight using the load cell and is therefore independent of pouch pressure. Second, the origami joint and the display's top surface are mechanically decoupled: the joint provides only vertical, single-degree-of-freedom motion of the platform, whereas contact area arises from local, fluid-driven wrapping of the top membrane around the fingertip. Pressurizing the pouch changes the platform's resistance to global vertical displacement (i.e., the rendered stiffness), but does not directly alter the local membrane–fluid geometry governing the wrap at a given water volume. Third, the contact-area response saturates with force. As shown in Figure 5H, the maximum contact area is reached at fingertip forces above approximately 2 N for all water volumes. Thus, differences in indentation depth resulting from varying stiffness settings are expected to have only a limited effect on contact area over the force range relevant to stiffness rendering. Any residual indirect coupling is therefore expected to be small relative to the volume-driven modulation of Figure 5H, thereby supporting independent control of the contact area and stiffness cues.

4.3.4.2 | Coupling Between Thermal and Softness Modules. The potential effect of temperature on the structural behavior of the bellows was evaluated using reported TPU Young's modulus values of 5.52 MPa at 23°C and 4.4 MPa at 49°C. An Euler buckling analysis of a representative folding surface ($10 \times 50 \times 0.1$ mm) yielded critical loads of approximately 2.26×10^{-3} N and 1.80×10^{-3} N, respectively. Thus, although the TPU modulus decreases by approximately 20%, the resulting change in critical load remains at the millinewton scale, far below the forces applied during device operation. The folding faces are fully folded under load across the operating temperatures, as intended, and the finger force is predominantly carried by the water volume and the origami joint rather than by the TPU folding surfaces. Moreover, as the folds are pre-set at 80°C, well above the 15–40°C operating range, the folding faces hinge about the existing creases rather than undergo buckling, and their fold geometry is not expected to change during thermal operation.

The effect of temperature-induced water volume expansion was also considered. The water volume in the origami bellows is regulated by weight via the load cell, ensuring the water mass remains constant regardless of temperature. Between 15 and 40°C the density of water decreases from 999.1 to 992.2 kg/m^3, a volumetric expansion of only 0.7%, or approximately 0.35 mL at the maximum 50 g fill. Based on the contact-area characteristic in Figure 5H (0–250 mm^2 over 0–50 g), this volume corresponds to a contact-area variation less than 2 mm^2 (<1% of the rendering range), which is negligible relative to the rendering range.

The pneumatic pouch was considered separately because it primarily undergoes membrane tension during inflation rather than buckling. The pouch is fabricated as a heat-pressed composite of nylon fabric, TPU, and polytetrafluoroethylene (PTFE). Reported PTFE Young's modulus values decrease from 317 MPa at 23°C to 182 MPa at 50°C, slightly above the maximum temperature considered here, so the resulting estimate is conservative. At a constant membrane stress, this reduction in modulus would increase the strain of an isolated PTFE layer by a factor of approximately 1.74. This estimate likely overstates the change in pouch compliance because the PTFE layer is mechanically constrained by the nylon and TPU layers of the composite. Moreover, the rendered stiffness is regulated through closed-loop force and displacement feedback, allowing the internal pouch pressure to compensate for variations in material compliance. Consequently, temperature changes may alter the passive compliance of the pouch but are not expected to substantially affect the commanded stiffness response within the operating temperature range. Complete derivations for both analyzes are provided in Section S1.2.

Furthermore, variations in water volume change the thermal mass of the display and can therefore affect the settling time of the temperature response. However, the display temperature is regulated in closed loop using the thermistor located inside the origami bellows, such that the rendered steady-state temperature is independent of the water volume. The pneumatic pouch forms a separate, air-filled circuit. Even under the conservative assumption that inflating the pouch to 200 kPa transiently heats the enclosed air by several tens of kelvin, the heat capacity of the enclosed air (~0.02 J/K) is four orders of magnitude smaller than that of the 50 mL water volume (~209 J/K), so the resulting contribution to the water temperature remains on the order of 0.01°C or smaller. Thus, softness modules are not expected to have a measurable effect on thermal rendering.

4.3.4.3 | Coupling Between Texture and Softness Modules. The potential effect of the texture module on stiffness rendering was analytically assessed. The electrovibration layer generates forces of at most 25 mN in the lateral direction and 15 mN in the normal direction (Figure 5B,C). In comparison,

2365709x, 0, Downloaded from https://advanced.onlinelibrary.wiley.com/doi/10.1002/admt.71463 by Technical University Delft, Wiley Online Library on [23/11/2026]. See the Terms and Conditions (https://onlinelibrary.wiley.com/terms-and-conditions) on Wiley Online Library for rules of use; OA articles are governed by the applicable Creative Commons License

stiffness rendering involves forces on the order of 1–10 N. Hence, the electrostatic contribution to the normal load, and consequently to the force measured by the FSR in the stiffness control loop, is at most 1.5%. This contribution is an order of magnitude smaller than the ≈15% human discrimination threshold for stiffness [56]. Therefore, the texture module is not expected to measurably affect stiffness rendering within the operating range.

During operation, the hydraulic and pneumatic systems deform the display surface: the fingertip pressure against the origami bellows deflects the top membrane, which in turn bends the flexible electrovibration layer. As the magnitude of the electrovibration force depends on the properties of the insulating layer, we experimentally quantified the effect of this bending. An epoxy (insulator) sample sandwiched between thin iron plates was bent to radii of curvature of 20, 40, 60, 80, and 100 mm, as well as a flat condition, and its capacitance was measured as a proxy for the insulator properties (Section S1.3 and Figure S3). Even at the smallest radius of 20 mm—more severe than any deflection occurring during device operation—the capacitance increased by only 3.59% relative to the flat sample. As the electrostatic force scales with the square of the coupling capacitance, this value corresponds to a force variation of approximately 7%, which is small relative to the force differences that can be produced.

4.3.4.4 | Coupling Between Texture and Thermal Modules. The potential influence of temperature on electrovibration was considered through the temperature dependence of the dielectric properties of the epoxy insulating layer. The dielectric constant of epoxy exhibits only weak temperature dependence below its glass-transition temperature (approximately 75°C), with a pronounced change occurring only at higher temperatures. As the operating temperature range of the display (15–40°C) remains well below the glass-transition temperature, resulting variation in the capacitance of the epoxy layer, and consequently in the generated electrovibration force, is expected to be negligible. The complete analysis is provided in Section S1.4.

4.3.4.5 | Coupling Between Actuation and Sensing Devices. The sensors of the stiffness control loop are physically isolated from the water circuit by design. The magnetometer and the sensing magnet are located outside the hydraulic circuit and separated from the water by the sealed bellows wall. As the water is non-magnetic, variations in water volume do not directly affect the magnetic field measurement. Furthermore, the origami joint carrying the magnet is mechanically decoupled from the top membrane: changing the water volume deforms the membrane but does not directly displace the magnet, and therefore cannot produce a spurious displacement reading. The FSR is likewise sealed from the bellows interior and does not contact the water. The water weight is supported by the bellows and its base, and it contributes only a small constant hydrostatic load (< 0.5 kPa), which is absorbed by the closed-loop force control.

The displacement sensing relies on the magnetic field of the NdFeB magnet embedded in the origami joint. The reversible temperature coefficient of remanence of NdFeB is approximately −0.11%/°C (as distinct from irreversible demagnetization, which is not expected to occur within this operating range). Across the 15–40°C operating range, this value corresponds to a maximum field variation of approximately 2.8% relative to room-temperature calibration. This number represents an upper bound, as the magnet is not in direct contact with the water circuit and is expected to experience a smaller temperature change than the display surface. Assuming the mapping from magnetic field to displacement reading, and in turn to rendered stiffness, is approximately linear over this range, a 2.8% field variation corresponds to a comparably small stiffness error, well below the 15% [56] stiffness discrimination threshold. Thermal effects on the magnetic displacement measurement are therefore not expected to compromise stiffness rendering.

The potential coupling between electrovibration actuation and the thermal sensing circuit was assessed analytically. The displacement current through the finger–electrode interface was not measured directly but was bounded by the insulator capacitance measured between two metal electrodes for Figure S3 (C = 2.73 nF). This value overestimates the effective finger–electrode coupling capacitance as the fingertip covers only part of the electrode area and the skin introduces an additional series capacitance. Using $I = 2\pi f C V_{\mathrm{rms}}$ at 70.7 V RMS (200 V_{pp}), the current was bounded by 0.16 mA at 128 Hz and 1.2 mA at 1000 Hz (Section S1.5). We used 1.2 mA as a conservative worst-case estimate, combining the highest characterized frequency, the maximum drive amplitude, and a capacitance that overestimates the finger–electrode coupling.

First, for resistive heating, 1.2 mA at 70.7 V RMS corresponds to an apparent power of approximately 85 mW. The actual dissipated power is lower because the current is predominantly capacitive. Even under the conservative assumption that the full apparent power were deposited as heat into the hydraulic circuit, whose 50 mL water volume has a heat capacity of approximately 209 J K^{-1}, the water temperature would increase by less than 4.1×10^{-4} °C s^{-1}, corresponding to approximately 0.016 °C over the 40 s measurement window. This value is below the ≈0.02 °C per-count resolution of the thermistor readout and well below the reported human thermal detection thresholds [67].

Second, for electrical pickup, the displacement current returns through the participant's grounding wristband rather than through the thermistor circuit. The thermistor leads are separated from the ITO electrode by the TPU bellows wall and multiple dielectric layers, limiting capacitive coupling into the readout. Any coupled component is an alternating signal at the drive frequency (≥28 Hz), whereas the thermal controller and hydraulic actuators operate at substantially lower bandwidths (below 1 Hz; Figure 5K). Such high-frequency pickup therefore should not alter the steady-state temperature estimate, although it could appear as a small oscillatory component in the recorded signal. The complete derivation is provided in the Section S1.5.

We also experimentally verified that the texture module's electric field does not measurably interfere with the magnetometer. The electrovibration voltage is applied between the fingertip and the top ITO layer, whereas the magnetometer is located below the origami joint, separated by multiple dielectric layers and the enclosed hydraulic chamber. Across all tested conditions, no systematic bias in the magnetometer output was observed beyond sensor noise. Thus, within the tested operating range, electrovibration does not measurably affect the displacement sensing.

2365709x, 0, Downloaded from https://advanced.onlinelibrary.wiley.com/doi/10.1002/admt.71463 by Technical University Delft, Wiley Online Library on [23/11/2026]. See the Terms and Conditions (https://onlinelibrary.wiley.com/terms-and-conditions) on Wiley Online Library for rules of use; OA articles are governed by the applicable Creative Commons License

4.4 | Psychophysical Experiments

4.4.1 | Participants

Thirteen participants (seven males and six females), aged 24 to 29, were recruited for the experiment. All participants were right-handed and had no history of sensory-motor disabilities. They were all students or employees at TU Delft with different backgrounds. Before the experiment, the participants were informed about the research intention and the experiment procedure. Then they all signed a consent form to confirm their voluntary participation. The experimental protocol complied with the Declaration of Helsinki and was approved by the Human Research Ethics Committee of TU Delft (application number 4545).

4.4.2 | Stimuli

The stimuli consisted of virtual surfaces rendered using our soft haptic device. These surfaces were generated using six physical parameters that governed roughness, friction, softness, and temperature. The parameters (Table S1) were carefully chosen to produce the most distinct textures possible while staying within the device's physical limits. In total, we had 64 distinct stimuli, each having a different parameter combination.

4.4.3 | Apparatus and Procedure

Two LCDs were used: one displayed only the graphical user interface for participants, while the other presented a control panel for experimenters. Participants wore headphones playing pink noise at a self-selected comfortable volume to minimize auditory distractions. They also wore a grounding wristband on their dominant arm to enhance the electrovibration sensation. Participants provided their responses using a mouse with their non-dominant hand.

Before the main experiments, participants washed their hands with soap and water and then dried them at room temperature. Then, they completed a brief, three-minute trial session, exploring four virtual surfaces rendered sequentially by the device. This trial session allowed participants to freely interact with the device and become familiar with the rendered sensations.

In the main experiment, the participant's task was to interact with the haptic device and rate the perceived sensation of 64 rendered virtual textures on eight adjective pairs: rough–smooth, flat–bumpy, sticky–slippery, warm–cold, regular–irregular, fine–coarse, hard–soft, and wet–dry. We selected these pairs as they were found to be the most relevant adjectives for surface perception in the previous literature [13, 24]. The participants rated their perception using a 9–point Likert scale for each pair. The total duration of the experiment was approximately 1.5 h. The experiment was divided into two sessions, each containing 32 stimuli to avoid fatigue.

During the experiment, the participants sat upright in front of the device while an experimenter sat beside them. The experiment started with a verbal notification from the experimenter. At the beginning of each stimulus, participants first saw a 5-second countdown clock on the GUI, indicating the preparation time before touching the haptic device. After 5 s, a graphical animation consisting of a red ball (representing the finger) and a transparent rectangle (representing the device) appeared in the top-right corner of the GUI. The movement of the red ball indicated the finger motions that the participants needed to follow. Following the texture rendering methodology proposed by Cozcolluela and Vardar [41], the participants moved their index finger to track the red ball's movement, performing three types of exploration patterns: static touch, sliding, and pressing, respectively, each lasting for 5 s. When the exploration time finished, the adjective scales on the LCD were enabled, allowing participants to rate their answers by using a computer mouse with their left (non-dominant) hand. The answering time lasted from 30 s to 1 min. After giving their ratings, participants clicked submit and returned the mouse back to the experimenter, who immediately initiated the next stimulus.

The recorded data were analyzed using principal component analysis (PCA) followed by factor analysis, as detailed in Refs. [24, 68].

Author Contributions

H.J. conceptualization, methodology, software, formal analysis, investigation (fabrication and control of the soft multimodal haptic device, design of the electrovibration surface, conducting user study), visualization, and writing – original draft. **K.L**. conceptualization, methodology, software, formal analysis, investigation (design and control of the hydraulic system, design of the electrovibration surface, programming and conducting user study), writing – original draft. **P.G.P**. methodology, investigation (cross–module characterization), formal analysis, visualization, and writing – review & editing. **Y.V**. conceptualization, methodology, formal analysis, writing – original draft, writing – review & editing, supervision, and funding acquisition.

Declaration of Generative AI and AI-Assisted Technologies in the Writing Process

The authors used OpenAI's ChatGPT and Grammarly Inc.'s Grammarly tool to enhance the language and readability of this work. After using these tools, the authors carefully reviewed and edited the content as needed. They take full responsibility for the final publication.

Funding

This work was partly funded by European Research Council (SuperTouch, 101220242) and Dutch Research Council (19153 and OCENW.XS23.1.178).

Conflicts of Interest

The authors declare no conflicts of interest.

Data Availability Statement

The data that supports the findings of this study can be requested from the corresponding author.

References

1. S. J. Lederman and R. L. Klatzky, "Extracting Object Properties Through Haptic Exploration," *Acta Psychologica* 84, no. 1 (1993): 29–40, https://doi.org/10.1016/0001-6918(93)90070-8, Tactile Pattern Recognition.

2365709x, 0, Downloaded from https://advanced.onlinelibrary.wiley.com/doi/10.1002/admt.71463 by Technical University Delft, Wiley Online Library on [23/11/2026]. See the Terms and Conditions (https://onlinelibrary.wiley.com/terms-and-conditions) on Wiley Online Library for rules of use; OA articles are governed by the applicable Creative Commons License

2. B. A. Richardson, Y. Vardar, C. Wallraven, and K. J. Kuchenbecker, "Learning to Feel Textures: Predicting Perceptual Similarities From Unconstrained Finger-Surface Interactions," *IEEE Transactions on Haptics* 15, no. 4 (2022): 705–717, https://doi.org/10.1109/TOH.2022.3212701.

3. A.-S. Augurelle, A. M. Smith, T. Lejeune, and J.-L. Thonnard, "Importance of Cutaneous Feedback in Maintaining a Secure Grip During Manipulation of Hand-Held Objects," *Journal of Neurophysiology* 89, no. 2 (2003): 665–671, https://doi.org/10.1152/jn.00249.2002.

4. A. Gallace and C. Spence, "The Science of Interpersonal Touch: An Overview," *Neuroscience and Biobehavioral Reviews* 34, no. 2 (2010): 246–259, https://doi.org/10.1016/j.neubiorev.2008.10.004, Touch, Temperature, Pain/Itch and Pleasure.

5. S. Biswas and Y. Visell, "Emerging Material Technologies for Haptics," *Advanced Materials Technologies* 4, no. 4 (2019): 1900042, https://doi.org/10.1002/admt.201900042.

6. O. Bau, I. Poupyrev, A. Israr, and C. Harrison, "TeslaTouch: Electrovibration for Touch Surfaces," in *Proceedings of the 23nd annual ACM symposium on User Interface Software and Technology* (2010), 283–292.

7. D. J. Meyer, M. Wiertlewski, M. A. Peshkin, and J. E. Colgate, "Dynamics of Ultrasonic and Electrostatic Friction Modulation for Rendering Texture on Haptic Surfaces," in *2014 IEEE Haptics Symposium (HAPTICS)* (2014), 63–67.

8. H.-N. Ho and L. A. Jones, "Modeling the Thermal Responses of the Skin Surface During Hand-Object Interactions," *Journal of Biomechanical Engineering* 130, no. 2 (2008): 021005, https://doi.org/10.1115/1.2899574.

9. L. Peters, G. Serhat, and Y. Vardar, "ThermoSurf: Thermal Display Technology for Dynamic and Multi-Finger Interactions," *IEEE Access* 11 (2023): 12004–12014, https://doi.org/10.1109/ACCESS.2023.3242040.

10. M. Mete, H. Jeong, W. D. Wang, and J. Paik, "SORI: A Softness-Rendering Interface to Unravel the Nature of Softness Perception," *Proceedings of the National Academy of Sciences* 121, no. 13 (2024): e2314901121.

11. E. P. Scilingo, M. Bianchi, G. Grioli, and A. Bicchi, "Rendering Softness: Integration of Kinesthetic and Cutaneous Information in a Haptic Device," *IEEE Transactions on Haptics* 3, no. 2 (2010): 109–118, https://doi.org/10.1109/TOH.2010.2.

12. H. Culbertson and K. J. Kuchenbecker, "Importance of Matching Physical Friction, Hardness, and Texture in Creating Realistic Haptic Virtual Surfaces," *IEEE Transactions on Haptics* 10, no. 1 (2017): 63–74, https://doi.org/10.1109/TOH.2016.2598751.

13. S. Okamoto, H. Nagano, and Y. Yamada, "Psychophysical Dimensions of Tactile Perception of Textures," *IEEE Transactions on Haptics* 6, no. 1 (2013): 81–93, https://doi.org/10.1109/TOH.2012.32.

14. L. Zou and Y. Vardar, "Learning to Feel Materials From Multisensory Tactile Data via Interpretable Models," (2026), preprint, bioRxiv, May 28, 2026, https://doi.org/10.48550/arXiv.2605.29572.

15. E. Baumgartner, C. B. Wiebel, and K. R. Gegenfurtner, "Visual and Haptic Representations of Material Properties," *Multisensory Research* 26 (2013): 429–455.

16. S. Mintchev, M. Salerno, A. Cherpillod, S. Scaduto, and J. Paik, "A Portable Three-Degrees-of-Freedom Force Feedback Origami Robot for Human–Robot Interactions," *Nature Machine Intelligence* 1 (2019): 584–593, https://doi.org/10.1038/s42256-019-0125-1.

17. Z. Zhang, Z. Xu, L. Emu, et al., "Active Mechanical Haptics With High-Fidelity Perceptions for Immersive Virtual Reality," *Nature Machine Intelligence* 5 (2023): 1–13, https://doi.org/10.1038/s42256-023-00671-z.

18. S. Follmer, D. Leithinger, A. Olwal, A. Hogge, and H. Ishii, "inFORM: Dynamic Physical Affordances and Constraints Through Shape and Object Actuation," in *Proceedings of the 26th Annual ACM Symposium on User Interface Software and Technology*, UIST '13 (Association for Computing Machinery, 2013), 417–426.

19. Q. Wu, J. Li, H. Seifi, and K. Hornbæk, "Vipins: Combining a Pin Array and Vibrotactile Actuators to Render Complex Shapes and Textures," *International Journal of Human-Computer Studies* 197 (2025): 103464, https://doi.org/10.1016/j.ijhcs.2025.103464.

20. R. V. Grigorii, J. E. Colgate, and R. Klatzky, "The Spatial Profile of Skin Indentation Shapes Tactile Perception Across Stimulus Frequencies," *Scientific Reports* 12 (2022): 13185, https://doi.org/10.1038/s41598-022-17324-7.

21. T. Liang, S. Guo, B. Cheng, Z. Xue, H. Zhang, and H. Xu, "ArrayTac: A Tactile Display for Simultaneous Rendering of Shape, Stiffness and Friction," preprint, bioRxiv, October 26, 2026, https://doi.org/10.48550/arXiv.2603.13829.

22. S. E. Emgin, A. Aghakhani, T. M. Sezgin, and C. Basdogan, "HapTable: An Interactive Tabletop Providing Online Haptic Feedback for Touch Gestures," *IEEE Transactions on Visualization and Computer Graphics* 25, no. 9 (2019): 2749–2762, https://doi.org/10.1109/tvcg.2018.2855154.

23. X. Guo, Y. Zhang, W. Wei, W. Xu, and D. Wang, *ThermalTex: A Two-Modal Tactile Display for Delivering Surface Texture and Thermal Information* (Springer, 2020), pp. 288–296.

24. B. L. Kodak and Y. Vardar, "FeelPen: A Haptic Stylus Displaying Multimodal Texture Feels on Touchscreens," *IEEE/ASME Transactions on Mechatronics* 28, no. 5 (2023): 2930–2940, https://doi.org/10.1109/TMECH.2023.3264787.

25. A. Talhan, S. Kumar, H. Kim, W. Hassan, and S. Jeon, "Multi-Mode Soft Haptic Thimble for Haptic Augmented Reality Based Application of Texture Overlaying," *Displays* 74 (2022): 102272.

26. M. S. Hashem, J. B. Joolee, W. Hassan, and S. Jeon, "Soft Pneumatic Fingertip Actuator Incorporating a Dual Air Chamber to Generate Multi-Mode Simultaneous Tactile Feedback," *Applied Sciences* 12, no. 1 (2021): 175.

27. A. Talhan, H. Kim, and S. Jeon, "Tactile Ring: Multi-Mode Finger-Worn Soft Actuator for Rich Haptic Feedback," *IEEE Access* 8 (2019): 957–966.

28. H. A. Sonar, J.-L. Huang, and J. Paik, "Soft Touch Using Soft Pneumatic Actuator–Skin as a Wearable Haptic Feedback Device," *Advanced Intelligent Systems* 3, no. 3 (2021): 2000168.

29. A. Raza, W. Hassan, and S. Jeon, "Pneumatically Controlled Wearable Tactile Actuator for Multi-Modal Haptic Feedback," *IEEE Access* 12 (2024): 59485–59499.

30. S. Chen, L. Yu, W. Shen, et al., "Multimodal 5-DOF Stretchable Electromagnetic Actuators Toward Haptic Information Delivery," *Advanced Functional Materials* 34, no. 17 (2024): 2314515.

31. B. Kang, N. Zavanelli, G. N. Sue, et al., "A Flexible Skin-Mounted Haptic Interface for Multimodal Cutaneous Feedback," *Nature Electronics* 8, no. 9 (2025): 818–830, https://doi.org/10.1038/s41928-025-01443-w.

32. C. Son, K. Ko, H. J. Lee, et al., "A Flexible Multimodal Tactile Display Array for Virtual Shape and Texture," *Microsystem Technologies* 22 (2016): 2587–2594.

33. E. Leroy, R. Hinchet, and H. Shea, "Multimode Hydraulically Amplified Electrostatic Actuators for Wearable Haptics," *Advanced Materials* 32, no. 36 (2020): 2002564.

34. J. Hartcher-O'Brien, V. Mehta, N. Colonnese, et al., "Fingertip Wearable High-Resolution Electrohydraulic Interface for Multimodal Haptics," in *2023 IEEE World Haptics Conference (WHC)* (IEEE, 2023), 299–305.

35. C. W. Carpenter, M. G. Malinao, T. A. Rafeedi, et al., "Electropneumotactile Stimulation: Multimodal Haptic Actuators Enabled by a Stretchable Conductive Polymer on Inflatable Pockets," *Advanced Materials Technologies* 5, no. 6 (2020): 1901119.

36. S.-Y. Jang, M. Cho, H. Kim, et al., "Dynamically Reconfigurable Shape-Morphing and Tactile Display via Hydraulically Coupled Mergeable and Splittable PVC Gel Actuator," *Science Advances* 10, no. 39 (2024): eadq2024, https://doi.org/10.1126/sciadv.adq2024.

2365709x, 0, Downloaded from https://advanced.onlinelibrary.wiley.com/doi/10.1002/admt.71463 by Technical University Delft, Wiley Online Library on [23/11/2026]. See the Terms and Conditions (https://onlinelibrary.wiley.com/terms-and-conditions) on Wiley Online Library for rules of use; OA articles are governed by the applicable Creative Commons License

37. S. Tan, M. A. Peskhin, R. L. Klatzky, and J. E. Colgate, "Toward Human-Resolution Haptics: A High-Bandwidth, High-Density, Wearable Tactile Display," *Science Advances* 11, no. 47 (2025): eadz5937, https://doi.org/10.1126/sciadv.adz5937.

38. C. V. Keef, L. V. Kayser, S. Tronboll, et al., "Virtual Texture Generated Using Elastomeric Conductive Block Copolymer in a Wireless Multimodal Haptic Glove," *Advanced Intelligent Systems* 2, no. 4 (2020): 2000018.

39. T. Han, F. Anderson, P. Irani, and T. Grossman, "HydroRing: Supporting Mixed Reality Haptics Using Liquid Flow," in *Proceedings of the 31st Annual ACM Symposium on User Interface Software and Technology*, UIST '18 (Association for Computing Machinery, 2018), 913–925.

40. Z. Sun, M. Zhu, X. Shan, and C. Lee, "Augmented Tactile-Perception and Haptic-Feedback Rings as Human-Machine Interfaces Aiming for Immersive Interactions," *Nature Communications* 13, no. 1 (2022): 5224.

41. A. Sanz Cozcolluela, K. Wösten, and Y. Vardar, "Generating Multimodal Textures With a Soft Hydro-Pneumatic Haptic Ring," *International Journal of Human-Computer Studies* 212 (2026): 103814, https://doi.org/10.1016/j.ijhcs.2026.103814.

42. S. Gallo, C. Son, H. J. Lee, H. Bleuler, and I.-J. Cho, "A Flexible Multimodal Tactile Display for Delivering Shape and Material Information," *Sensors and Actuators A: Physical* 236 (2015): 180–189.

43. Y. Huang, J. Zhou, P. Ke, et al., "A Skin-Integrated Multimodal Haptic Interface for Immersive Tactile Feedback," *Nature Electronics* 6 (2023): 1020–1031, https://doi.org/10.1038/s41928-023-01074-z.

44. H. Yi, H. Lee, and S. Yoon, "ThermicVib: Enabling Dynamic Thermal Sensation with Multimodal Haptic Glove for Thermal-Responsive Interaction," in *Proceedings - 2024 IEEE International Symposium on Mixed and Augmented Reality, ISMAR 2024*, eds. U. Eck, M. Sra, J. Stefanucci, M. Sugimoto, M. Tatzgern, and I. Williams (Institute of Electrical and Electronics Engineers Inc., 2024), 614–623.

45. T. Nozawa, R. Liu, and H. Sawada, "Displaying Tactile Sensation by SMA-Driven Vibration and Controlled Temperature for Cutaneous Sensation Assessment," *Actuators* 13 (2024): 463, https://doi.org/10.3390/act13110463.

46. Y. Vardar and K. J. Kuchenbecker, "Finger Motion and Contact by a Second Finger Influence the Tactile Perception of Electrovibration," *Journal of Royal Society Interface* 18, no. 176 (2021): 20200783, https://doi.org/10.1098/rsif.2020.0783.

47. M. A. Srinivasan and R. H. LaMotte, "Tactual Discrimination of Softness," *Journal of Neurophysiology* 73, no. 1 (1995): 88–101, https://doi.org/10.1152/jn.1995.73.1.88.

48. C. Dhong, R. Miller, N. B. Root, et al., "Role of Indentation Depth and Contact Area on Human Perception of Softness for Haptic Interfaces," *Science Advances* 5, no. 8 (2019): eaaw8845, https://doi.org/10.1126/sciadv.aaw8845.

49. Y. Vardar, B. Güçlü, and C. Basdogan, "Effect of Waveform on Tactile Perception by Electrovibration Displayed on Touch Screens," *IEEE Transactions on Haptics* 10, no. 4 (2017): 488–499, https://doi.org/10.1109/TOH.2017.2704603.

50. J. K. Balasubramanian, B. L. Kodak, and Y. Vardar, "SENS3: Multisensory Database of Finger-Surface Interactions and Corresponding Sensations," in *Haptics: Understanding Touch; Technology and Systems; Applications and Interaction*, eds. H. Kajimoto, P. Lopes, C. Pacchierotti, C. Basdogan, M. Gori, B. Lemaire-Semail, and M. Marchal (Springer Nature Switzerland, 2025), 262–277.

51. J. K. Balasubramanian, D. M. Pool, and Y. Vardar, "Sliding Speed Influences Electrovibration-Induced Finger Friction Dynamics on Touchscreens," *Tribology International* 213 (2026): 111054, https://doi.org/10.1016/j.triboint.2025.111054.

52. C. U. Kenanoglu, M. Wiertlewski, and Y. Vardar, "Electrostatic Actuation Induces Competing Adhesion and Vibration Regimes at Fingertip Contact," *Advanced Intelligent Systems* 8 (2026): e70433.

53. E. AliAbbasi, M. A. Sormoli, and C. Basdogan, "Frequency-Dependent Behavior of Electrostatic Forces Between Human Finger and Touch Screen Under Electroadhesion," *IEEE Transactions on Haptics* 15, no. 2 (2022): 416–428.

54. H. Z. Tan, N. I. Durlach, G. L. Beauregard, and M. A. Srinivasan, "Manual Discrimination of Compliance Using Active Pinch Grasp: The Roles of Force and Work Cues," *Perception and Psychophysics* 57, no. 4 (1995): 495–510, https://doi.org/10.3758/BF03213075.

55. M. Di Luca, B. Knörlein, M. O. Ernst, and M. Harders, "Effects of Visual–Haptic Asynchronies and Loading–Unloading Movements on Compliance Perception," *Brain Research Bulletin* 85, no. 5 (2011): 245–259, https://doi.org/10.1016/j.brainresbull.2010.02.009.

56. W. M. Bergmann Tiest and A. M. L. Kappers, "Cues for Haptic Perception of Compliance," *IEEE Transactions on Haptics* 2, no. 4 (2009): 189–199, https://doi.org/10.1109/TOH.2009.16.

57. S. Jeon and S. Choi, "Modulating Real Object Stiffness for Haptic Augmented Reality," in *International Conference on Human Haptic Sensing and Touch Enabled Computer Applications* (Springer, 2008), 609–618.

58. D. Filingeri, B. Redortier, S. Hodder, and G. Havenith, "The Role of Decreasing Contact Temperatures and Skin Cooling in the Perception of Skin Wetness," *Neuroscience Letters* 551 (2013): 65–69.

59. W. J. Adams, I. S. Kerrigan, and E. W. Graf, "Touch Influences Perceived Gloss," *Scientific Reports* 6, no. 1 (2016): 21866.

60. M. Park, J.-Y. Yoo, T. Yang, et al., "Skin-Integrated Systems for Power Efficient, Programmable Thermal Sensations Across Large Body Areas," *Proceedings of the National Academy of Sciences* 120, no. 6 (2023): e2217828120, https://doi.org/10.1073/pnas.2217828120.

61. Y. Jung, M. Kim, T. Kim, J. Ahn, J. Lee, and S. H. Ko, "Functional Materials and Innovative Strategies for Wearable Thermal Management Applications," *Nano-Micro Letters* 15 (2023): 160, https://doi.org/10.1007/s40820-023-01126-1.

62. K. Liu, J. Wang, X. Pan, et al., "N-Type Thermoelectric Elastomers," *Nature* 644 (2025): 920–926, https://doi.org/10.1038/s41586-025-09387-z.

63. B. Russ, A. Glaudell, J. J. Urban, M. L. Chabinyc, and R. A. Segalman, "Organic Thermoelectric Materials for Energy Harvesting and Temperature Control," *Nature Reviews Materials* 1 (2016): 16050, https://doi.org/10.1038/natrevmats.2016.50.

64. J. Jiao, D. Wang, Y. Zhang, et al., "Detection and Discrimination Thresholds for Haptic Gratings on Electrostatic Tactile Displays," *IEEE Transactions on Haptics* 12, no. 1 (2018): 34–42.

65. T. Tachi and K. Miura, "Rigid-Foldable Cylinders and Cells," *Journal of the International Association for Shell and Spatial Structures* 53, no. 4 (2012): 217–226.

66. J.-G. Lee and H. Rodrigue, "Origami-Based Vacuum Pneumatic Artificial Muscles With Large Contraction Ratios," *Soft Robotics* 6, no. 1 (2019): 109–117.

67. L. A. Jones and H.-N. Ho, "Warm or Cool, Large or Small? The Challenge of Thermal Displays," *IEEE Transactions on Haptics* 1, no. 1 (2008): 53–70, https://doi.org/10.1109/TOH.2008.2.

68. K. Drewing, C. Weyel, H. Celebi, and D. Kaya, "Systematic Relations Between Affective and Sensory Material Dimensions in Touch," *IEEE Transactions on Haptics* 11, no. 4 (2018): 611–622, https://doi.org/10.1109/TOH.2018.2836427.

Supporting Information

Additional supporting information can be found online in the Supporting Information section.

Supporting File: admt71463-sup-0001-SuppMat.pdf.

2365709x, 0, Downloaded from https://advanced.onlinelibrary.wiley.com/doi/10.1002/admt.71463 by Technical University Delft, Wiley Online Library on [23/11/2026]. See the Terms and Conditions (https://onlinelibrary.wiley.com/terms-and-conditions) on Wiley Online Library for rules of use; OA articles are governed by the applicable Creative Commons License